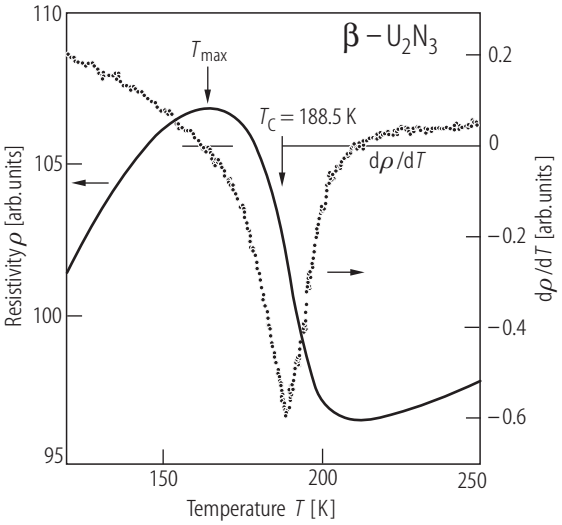

Fig. 228. β-U_2N_3. Electrical resistivity normalized to ρ(285K) = 100, (left-hand side scale) and its derivative, dρ/dT, (right-hand side scale) vs. temperature, T [87MST1]. The sample was prepared by a reaction annealing of pressed mononitride UN at 1350 ºC under nitrogen gas [82MT]. T_C = 188.5(4) K being in agreement with the values evaluated from magnetic measurements by [62TTL] and [72NTTK], but in disagreement with 235(5) K reported by [64AJD]. No explanation of the maximum in $\rho(T)$ at T_{max} = 163 K has been given.

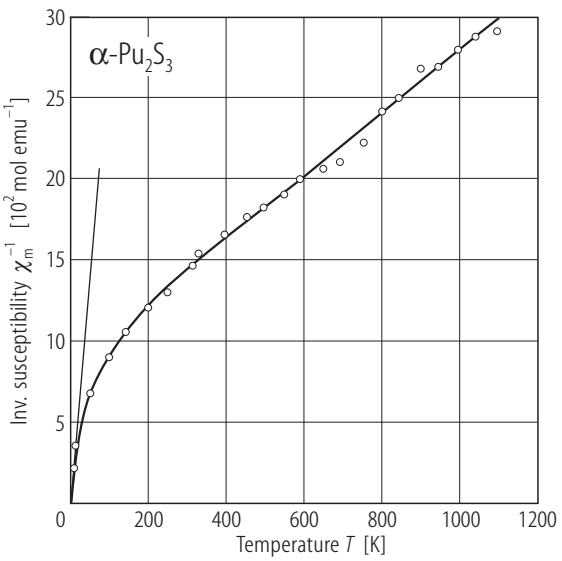

Fig. 230. α-Pu_2S_3. Inverse molar magnetic susceptibility, χ_m^{-1}, vs. temperature, T, up to 1100 K [69RD]. The solid curve is a guide for the eye. The thin straight line at low temperatures marks a slope corresponding to the magnetic moment p_{eff} = 0.56 μ_B. The experimental effective moment, calculated from the Curie-Weiss law above 200 K (p_{eff} = 2.06 μ_B, Θ = –650 K), is far too large for Pu^{3+}.

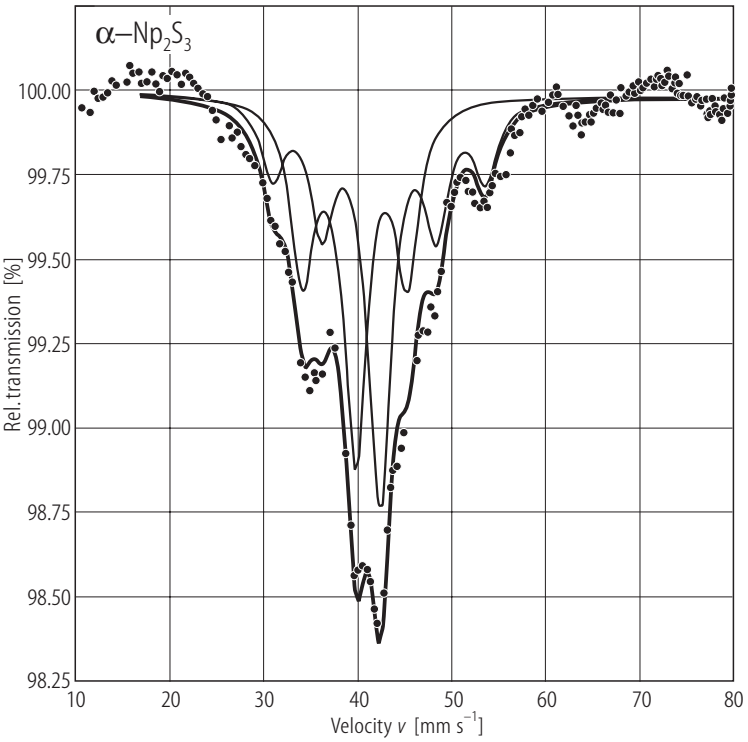

Fig. 229. α-Np_2S_3. ^{237}Np Mössbauer absorption spectrum taken at T = 4.2 K [84TJP]. The subspectra are drawn by thin solid lines. The hyperfine parameters are presented in Table J. On the basis of the two isomer shift values it is concluded that all Np ions are trivalent.

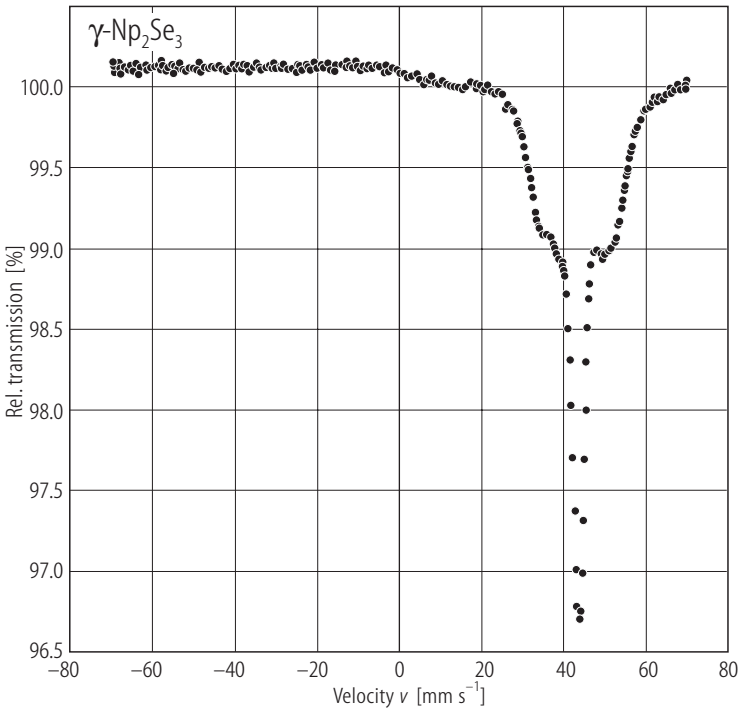

Fig. 231. γ-Np_2Se_3. ^{237}Np Mössbauer absorption spectrum taken at T = 4.2 K [84TJP]. The hyperfine parameters are presented in Table J. The isomer shift was calculated from the position of the central line. From its value it is concluded that Np ions are trivalent (see Introduction).

For Fig. 232 see next page

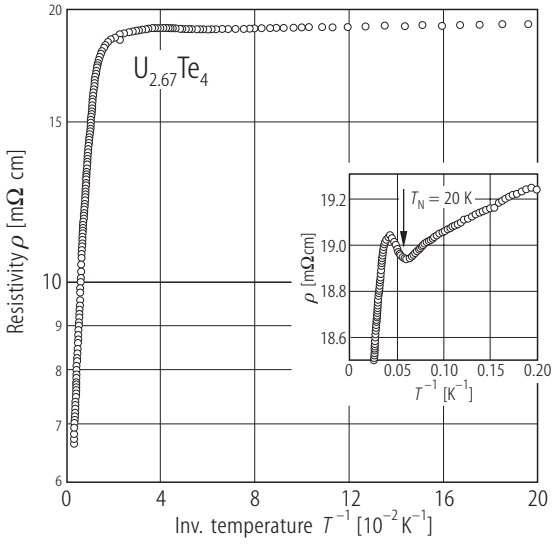

Fig. 233. $U_{2.67}Te_4$, sc. Resistivity, ρ, vs. inverse temperature, $1/T$, measured with the current flowing in the (110) plane [99ST]. The data for $90 < T < 170$ K follow the semiconducting activation formula with ΔE_g = 20 meV. In the interval $4.2 < T < 17$ K the data were analysed in terms of quasi-semiconducting properties according to the formula $\sigma(T) = \sigma_0(T) + \sigma_1 \exp(-\Delta E_g / 2k_B T)$. For details see the original paper. Inset: ρ vs. $1/T$ in the vicinity of the Néel temperature.

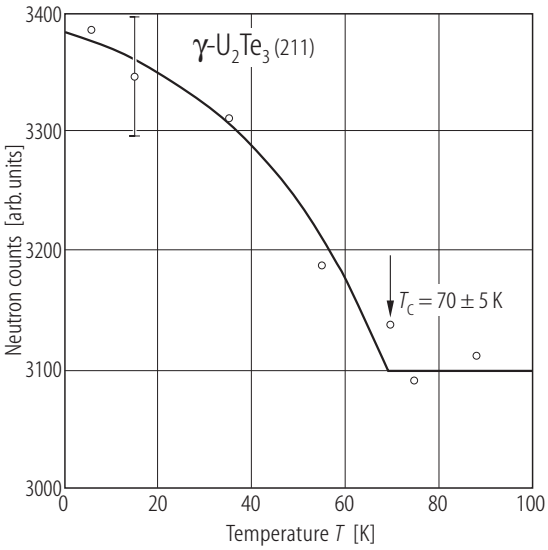

Fig. 234. γ-U_2Te_3. Magnetic contribution to the (211) peak intensity vs. temperature, T [82BRSJ]. The compound orders ferromagnetically at T_C = 70(5) K. The uranium magnetic moment at 15 K amounts to 1.78 μ_B. From powder neutron diffraction data it was impossible to determine the magnetic structure of this cubic compound. Note that in the literature there are large discrepancies in the T_C values from 38 K [72SMR] to 150 K [59TS]. This is probably related to differences in the compositions of cation-deficient $U_{3-y}Te_4$ compounds studied.

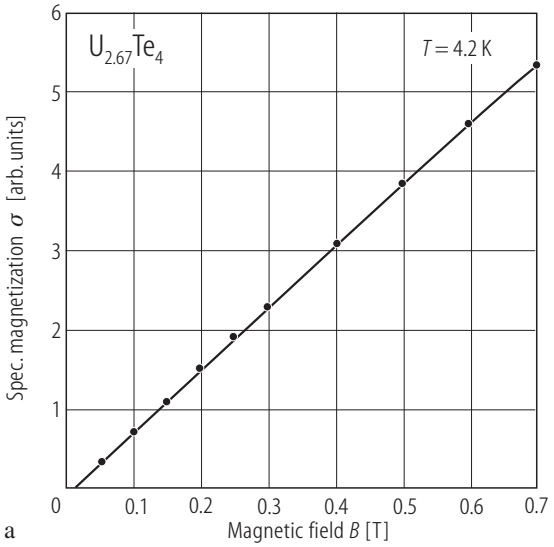

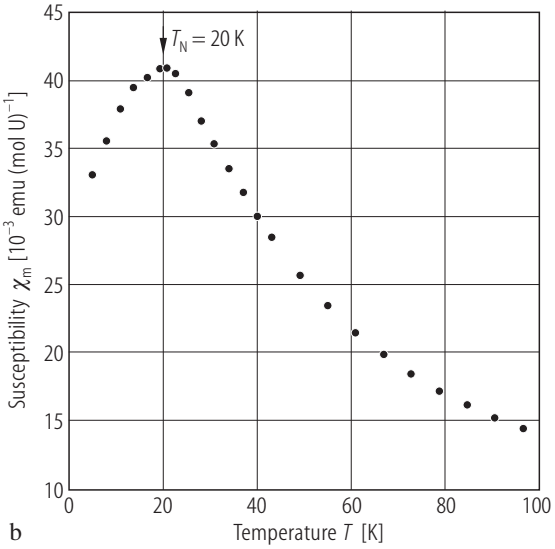

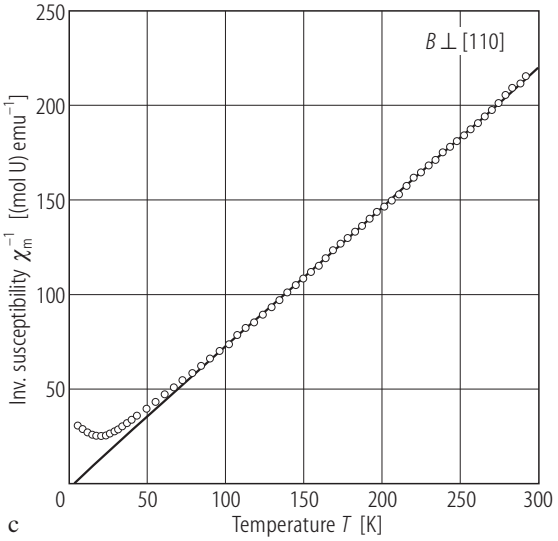

Fig. 232. $U_{2.67}Te_4$, sc. **(a)** Specific magnetization, σ, vs. magnetic field, B, taken at $T = 4.2$ K [95SSTK]. The straight-line behaviour with no hysteresis indicates an absence of ferromagnetic impurities. **(b)** Low temperature molar magnetic susceptibility, χ_m, vs. temperature, T [95SSTK]. The compound orders antiferromagnetically at $T_N = 20$ K. **(c)** Inverse molar magnetic susceptibility per U atom, χ_m^{-1}, vs. temperature, T, measured with $B \perp$ [110] [95SSTK]. The solid line is a Curie-Weiss fit with the parameters given in Table F.

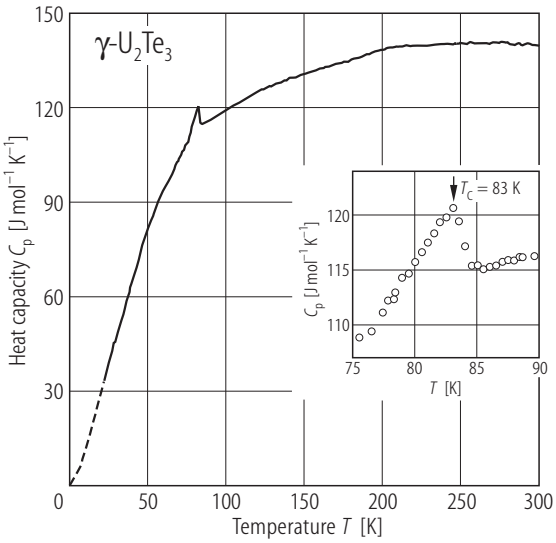

Fig. 235. U_2Te_3, sc. Heat capacity, C_p, vs. temperature, T, in the range 25…300 K [98PT]. The compound orders ferromagnetically at T_C = 83 K. Inset: C_p vs. T in the vicinity of T_C.

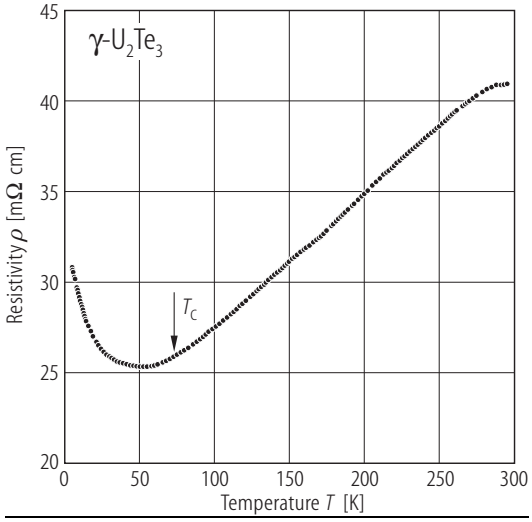

←

Fig. 236. γ-U_2Te_3. Electrical resistivity, ρ, vs. temperature, T [81BJS]. The compound is a semimetallic conductor with a change in the slope in $\rho(T)$ not far below $T_C \approx 80$ K.

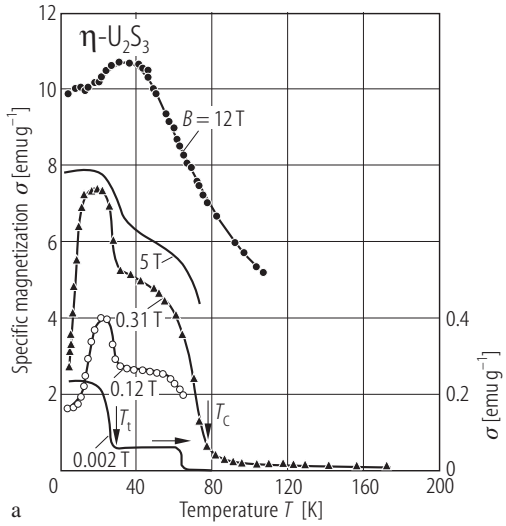

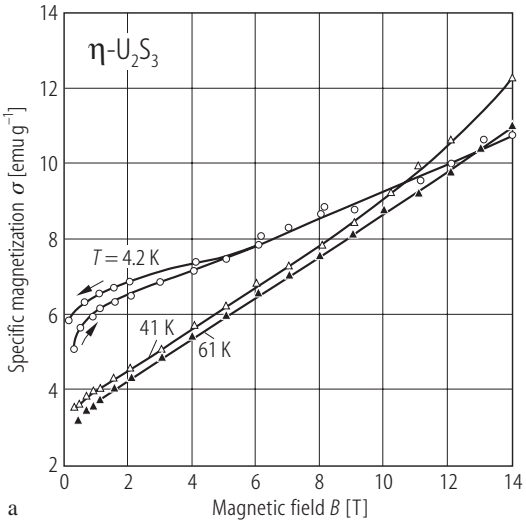

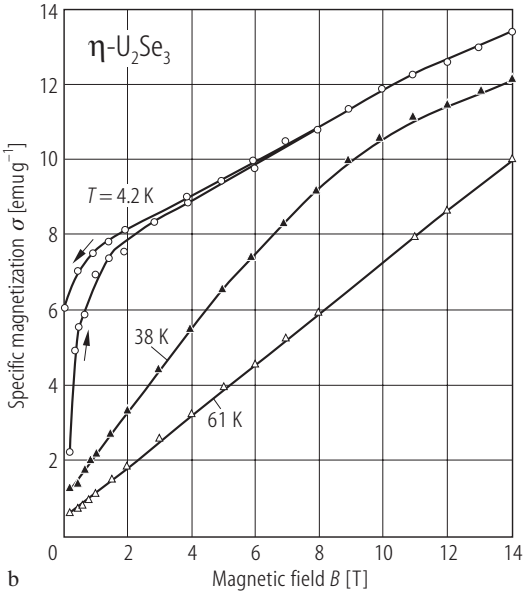

Fig. 237. η-U_2Y_3, Y = S, Se. Specific magnetization, σ, vs. magnetic field, B, up to 14 T taken at several selected temperatures [76SWBS]. **(a)** U_2S_3; **(b)** U_2Se_3.

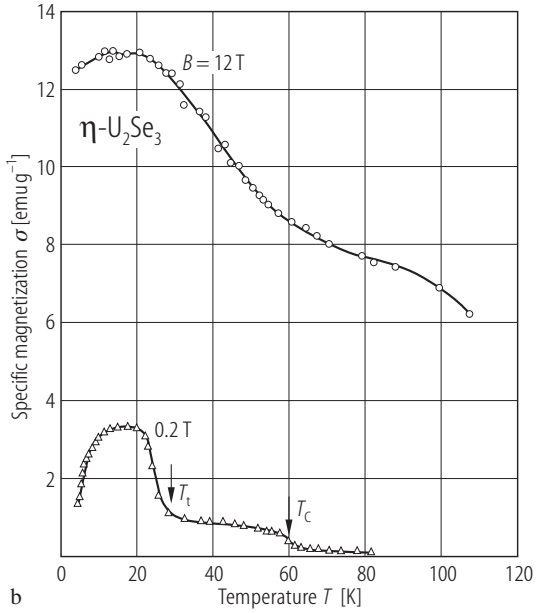

←

Fig. 238. η-U_2Y_3, Y = S, Se. Specific magnetization, σ, vs. temperature, T, taken at various magnetic fields [76SWBS]. **(a)** U_2S_3; **(b)** U_2Se_3. Note a complex magnetic character of both compounds, with possible ferrimagnetic order at low temperatures being favored by their orthorhombic crystal structure with two nonequivalent positions for U atoms.

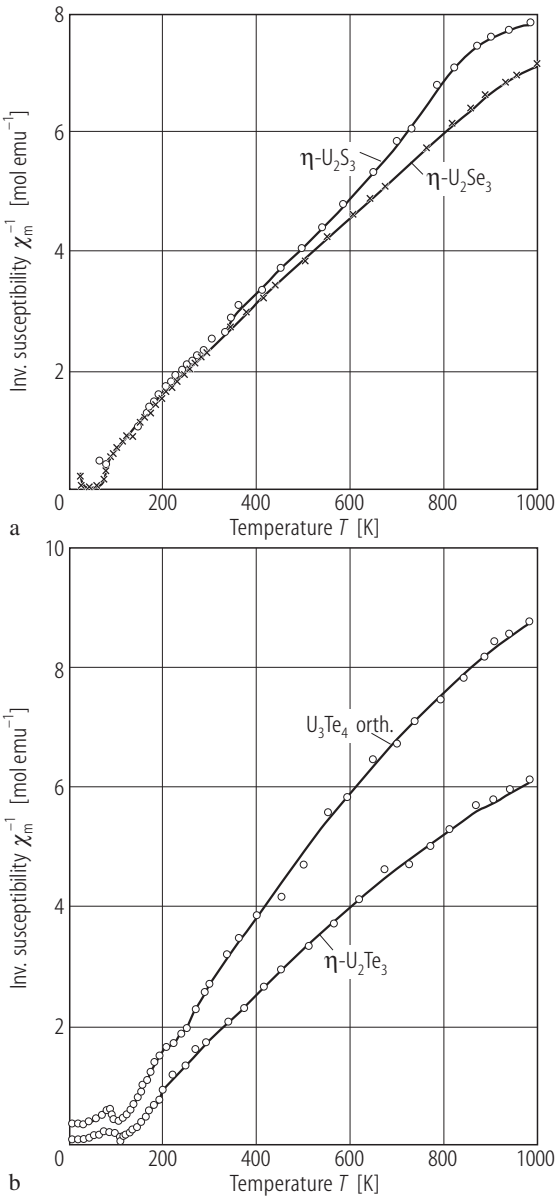

Fig. 239. η-U_2Y_3, Y = S, Se, Te. Inverse molar magnetic susceptibility, χ_m^{-1}, vs. temperature, T, up to 1000 K [76SWBS]. **(a)** U_2S_3 and U_2Se_3; **(b)** U_2Te_3 in comparison to ortho-U_3Te_4 phase.

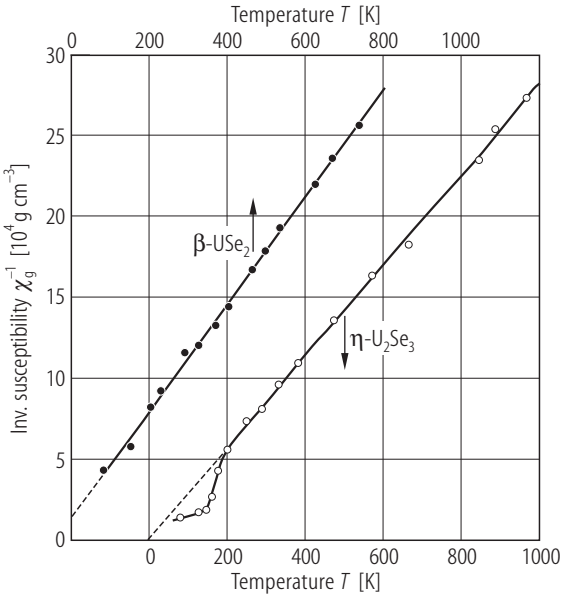

Fig. 240. η-U_2Se_3, β-USe_2. Inverse mass magnetic susceptibility, χ_g^{-1}, vs. temperature, T, up to ≈900 K [67CPYM]. Lower temperature scale: η-U_2Se_3; upper temperature scale: β-USe_2. The straight lines show the Curie-Weiss behavior with the fit parameters given in Table F.

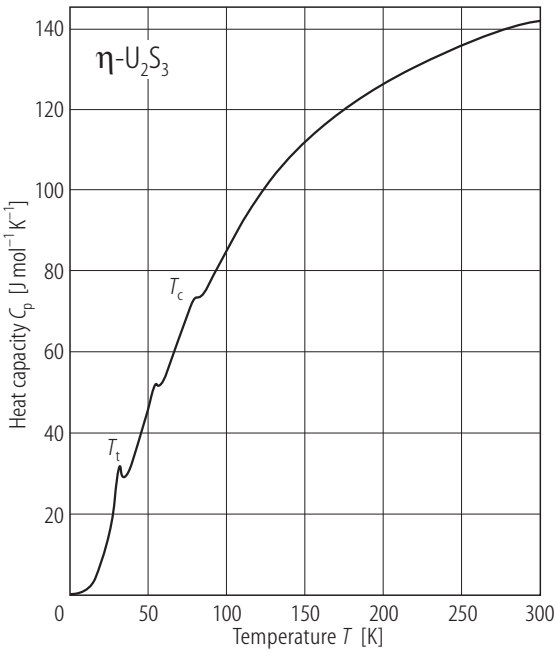

Fig. 241. η-U_2S_3. Heat capacity, C_p, vs. temperature, T, in the range 4…300 K [80LWSJ]. There are three small peaks at 30.6, 55.0 and 82.8 K. The former and the latter C_p-anomalies are probably due to magnetic phase transitions observed in the magnetization studies (see Fig. 238a).

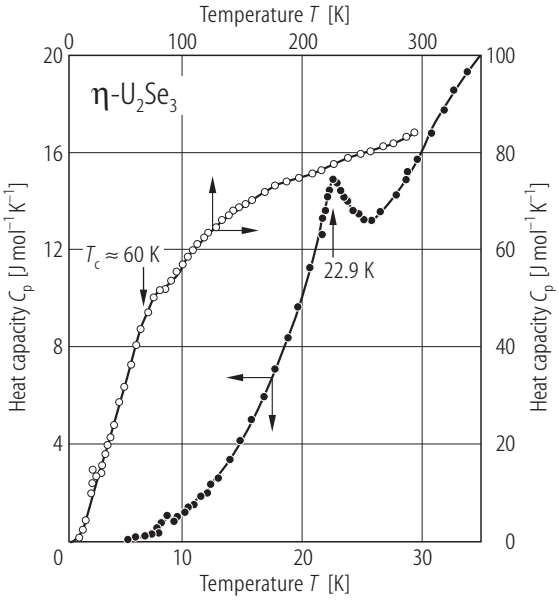

Fig. 242. η-U_2Se_3. Heat capacity, C_p, vs. temperature, T, in the range 5…300 K (right-hand and upper scales) and 5…38 K (left-hand and bottom scales) [75LSW]. A sharp peak at 22.9 K and a small more-diffused one at about 60 K correspond probably to magnetic phase transitions T_t and T_C evidenced in magnetization studies (see Fig. 238b). The other tiny anomaly at 8 K is not related to any singularity in $\sigma(T)$ and has unclear origin.

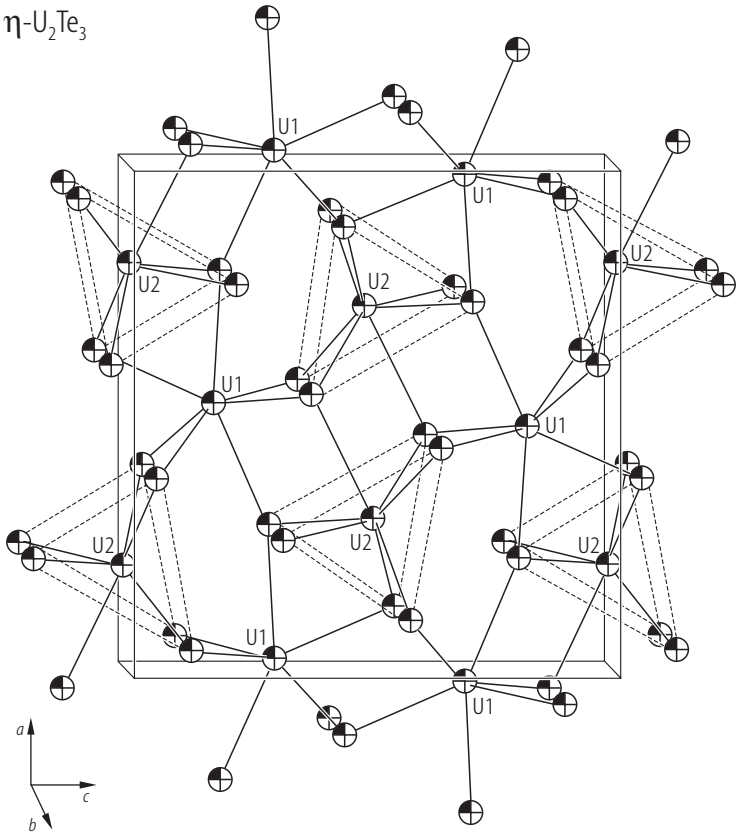

Fig. 243. η-U_2Te_3. Orthorhombic crystal structure of Sb_2S_3 type (space group Pnma) [98TPLN]. Note that two non-equivalent U atoms, U1 and U2, have different environments for tellurium. The coordination of U1 is sevenfold and forms an irregular octahedron with one apex split into two Te positions, while U2 has a monocapped trigonal prismatic 7-fold coordination as outlined by dashed lines.

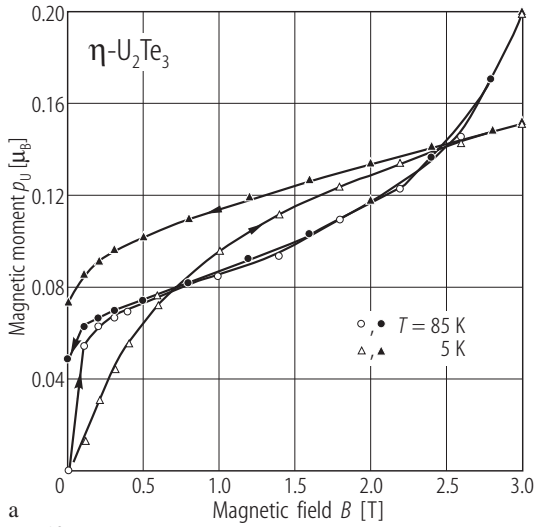

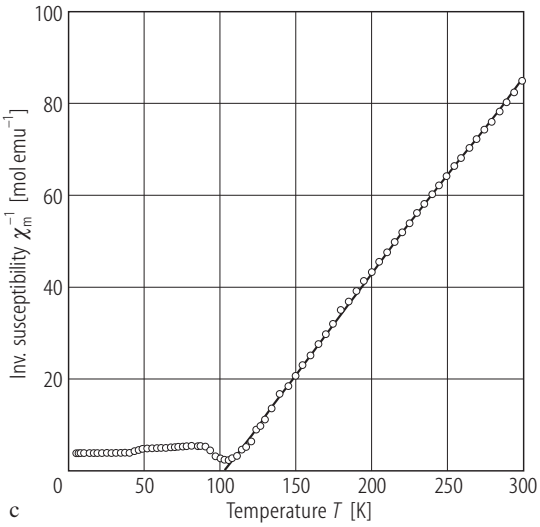

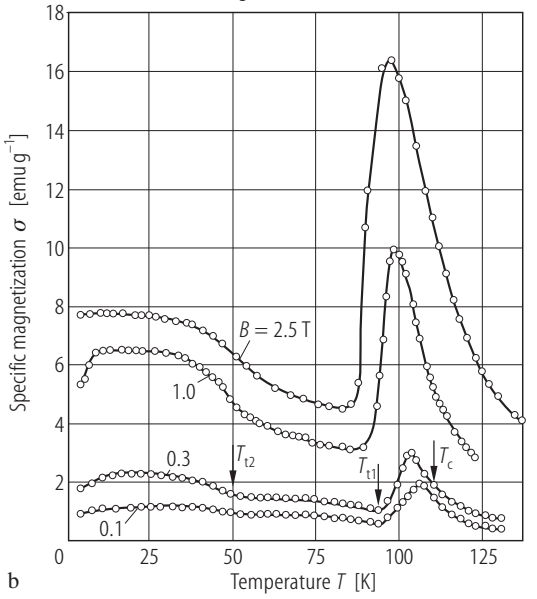

Fig. 244. η-U_2Te_3. **(a)** Magnetic moment, p_U, vs. magnetic field, B, taken at T = 5 K (triangles) and 85 K (circles) with increasing (open symbols) and decreasing (full symbols) magnetic field [98TPLN]. Note a significant rise in the magnetization above 2 T for p_U (B) taken at 85 K, suggesting a spin flip transition. **(b)** Specific magnetization, σ, vs. temperature, T, taken in various field strengths [80SJ]. The compound exhibits complex magnetic properties with an onset of ferromagnetic order at T_C = 110 K and two subsequent spin reorientations at 96 K and 50 K (see Fig. 247). **(c)** Inverse molar magnetic susceptibility, χ_m^{-1}, vs. temperature, T, measured in a field of 0.4 T [98TPLN]. The solid line is a modified Curie-Weiss fit with the parameters given in Table F.

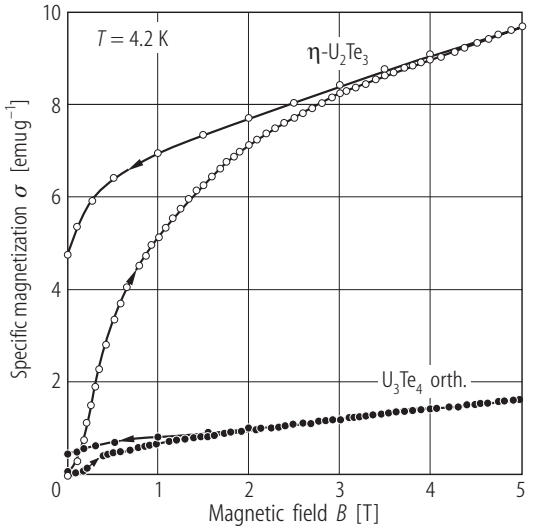

Fig. 245. η-U_2Te_3, ortho-U_3Te_4. Specific magnetization, σ, vs. magnetic field, B, taken at T = 4.2 K with increasing and decreasing magnetic field (as shown by the arrows) [80SJ]. Open circles: η-U_2Te_3; full circles: ortho-U_3Te_4. Note a ferromagnetic-like character of η-U_2Te_3 with $\sigma(B)$ typical of strongly anisotropic systems, and an almost linear behaviour of $\sigma(B)$ in strong magnetic fields observed for ortho-U_3Te_4.

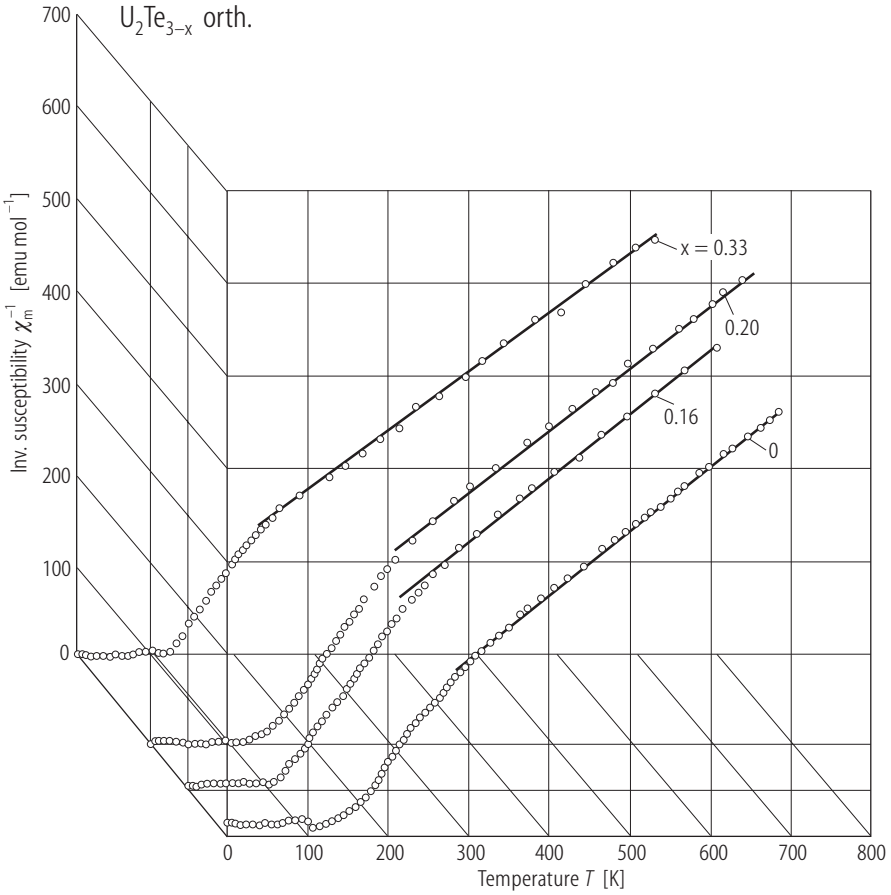

Fig. 246. U_2Te_{3-x}. Inverse molar magnetic susceptibility, χ_m^{-1}, vs. temperature, T up to 800 K for various x [82SJ]. The solid lines emphasize a straight-line behaviour of $\chi_m^{-1}(T)$ above 300…400 K. The nonlinear character of $\chi_m^{-1}(T)$ at lower temperatures points to a ferrimagnetic ordering in all these compositions occurring at about 105 K.

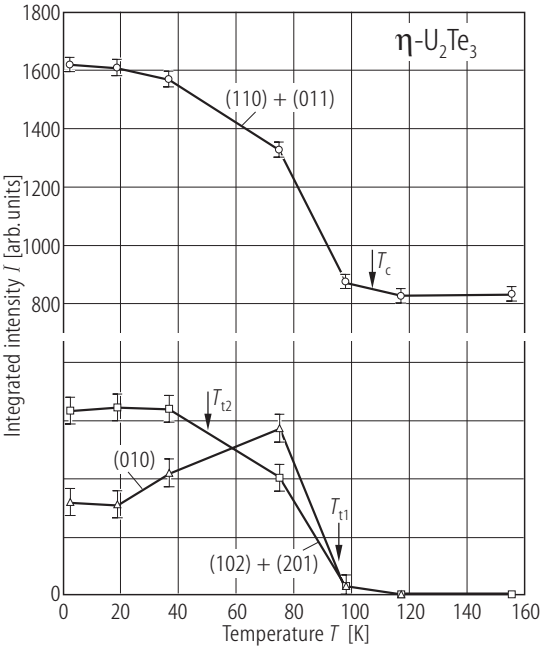

Fig. 247. η-U_2Te_3. Integrated neutron diffraction intensity, I, of some characteristic Bragg peaks vs. temperature, T, below 160 K [01TABN]. The compound orders magnetically below 110(5) K and exhibits two subsequent changes in the magnetic structure at 96(5) and 50(10) K (compare Fig. 244).

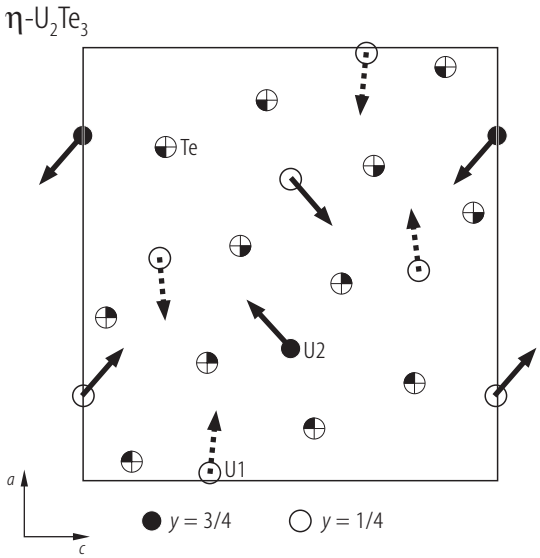

Fig. 248. η-U_2Te_3. Magnetic structure at 1.4 K projected on the (*ac*)-plane [01TABN]. Below T_C = 110 K the magnetic moments on two inequivalent U sites (marked by solid and dashed arrows) form a complex noncollinear structure within the (*ac*)-plane and have different amplitudes. At 1.4 K, the U1 (2.28 μ_B) and U2 (2.16 μ_B) moments have their components along the *a*-axis and the *c*-axis, coupled antiferromagnetically to each other but with different + and – sequences. In the vicinity of 50 K there occurs a spin reorientation on the U2 site towards the *c*-axis. Another spin arrangement type, but as yet being unresolved, occurs around 96 K (see Fig. 244b). Between 96 and 110 K short range spin correlations are superposed to a possibly modulated type of magnetic structure.

For Fig. 249 see next page

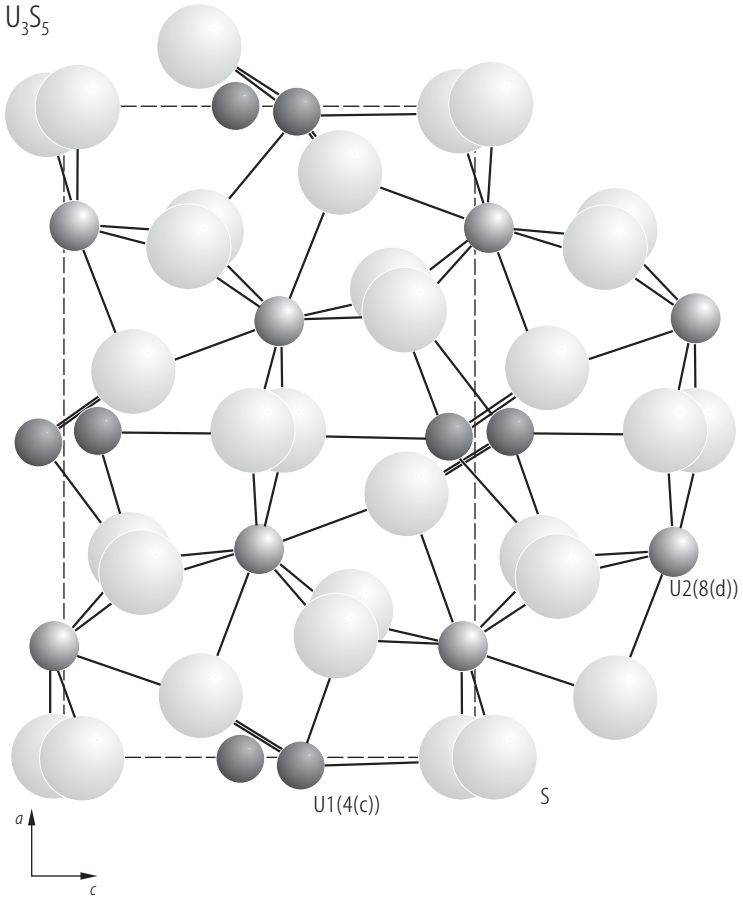

Fig. 250. U_3S_5. Orthorhombic crystal structure (space group Pnma) projected down the *b*-axis [80NP]. Dark small circles: U1 atoms at 4(c) sites; light small circles: U2 atoms at 8(d) sites; light large circles: S atoms. The U1 atoms have a 7-fold coordination to the S atoms, while the U2 atoms have an 8-fold such coordination. The U1 atom is lying within polyhedra related to an octahedron in which one apex is split into two positions. The U2 atom is in a monocapped trigonal prism. On the basis of crystal structure refinements of the compounds with the general formula MR_2S_5, where M = U, Zr, Hf and R = rare earth element, it was derived that the 4(c) positions are occupied by the M^{4+} ions while the 8(d) positions are occupied by the R^{3+} ions. The compound U_3S_5 can thus be represented as $U^{4+}(U^{3+})_2(S^{2-})_5$.

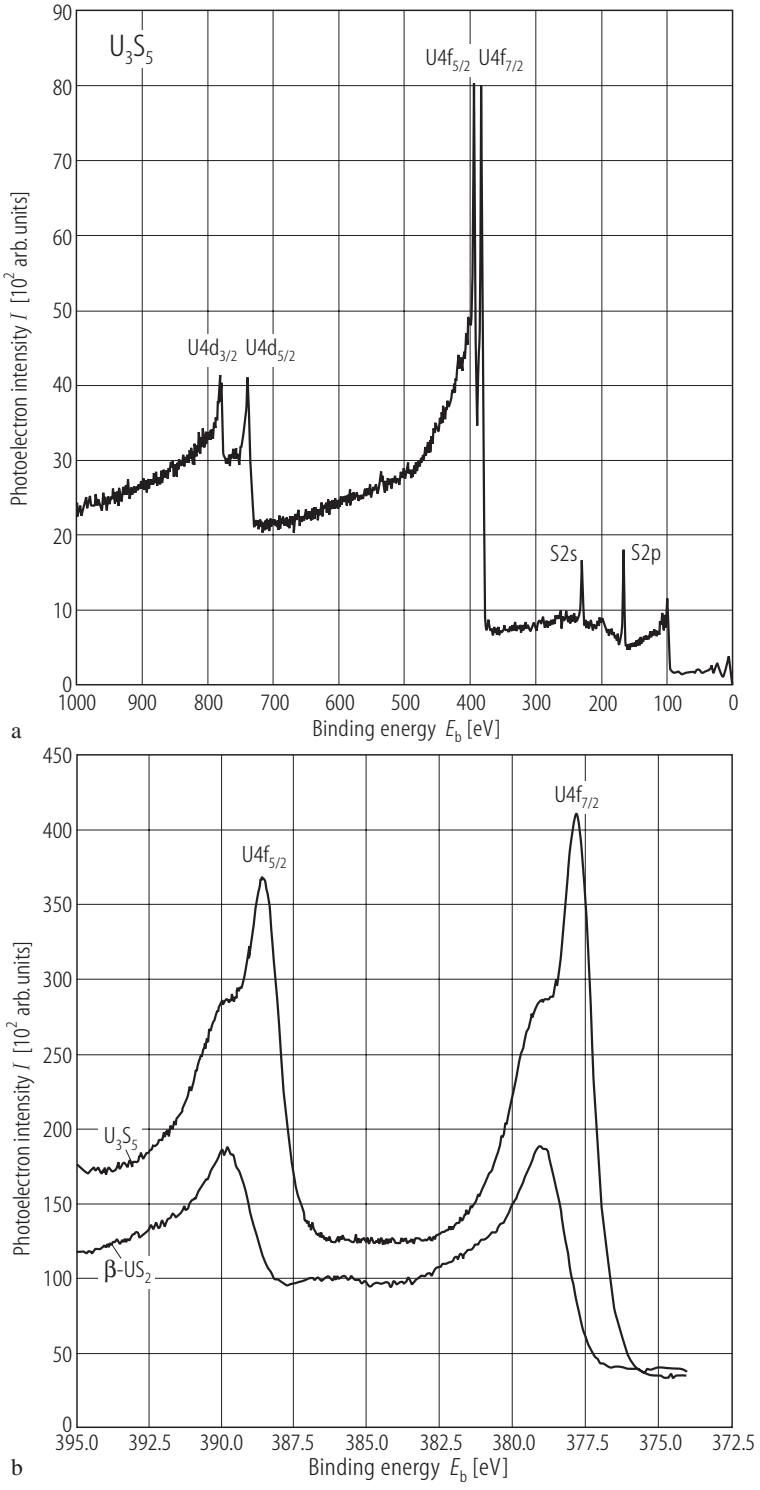

Fig. 249. U_3S_5, sc. **(a)** X-ray photoelectron spectra taken at T = 300 K [00KB]. **(b)** Uranium 4f core level spectra compared to those of β-US_2 [00KB]. The main peaks at binding energies 388.5 and 377.8 eV correspond to U $4f_{5/2}$ and U $4f_{7/2}$ signals of U^{3+} ions, respectively. The shoulders at 389.7 and 379.0 eV resemble the U $4f_{5/2}$ and U $4f_{7/2}$ peaks in β-US_2, which contains U^{4+} ions only. The XPS data give a direct evidence for two valence states of U ions in U_3Se_5, which can be rationalized by the formula $(U^{3+})_2$ U^{4+} $(Se^{2-})_5$. E_b relative to E_F.

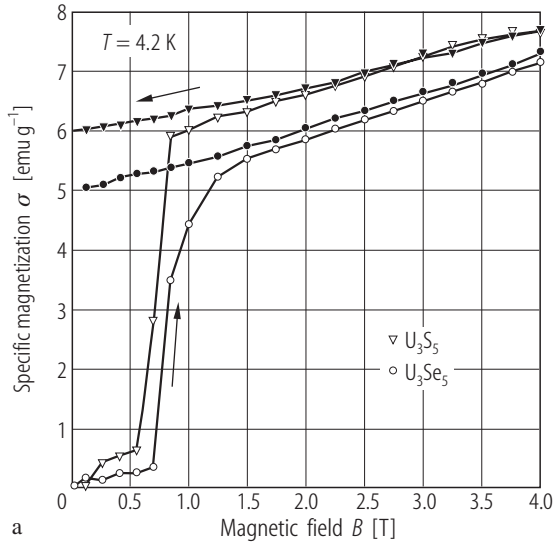

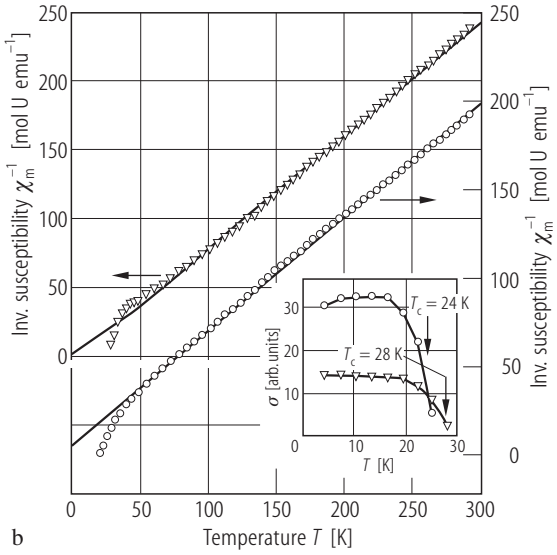

Fig. 251. U_3Y_5, Y = S, Se, sc. **(a)** Specific magnetization, σ, vs. magnetic field, B, taken at T = 4.2 K on a set of freely oriented single crystals with increasing (open symbols) and decreasing (full symbols) magnetic field [95S, 99ST]. Note a rapid increase in magnetization after overcoming a critical field B_c = 0.6…0.8 T, and its almost linear increase in higher applied magnetic fields. Similar behaviour was found in [74SR] on a polycrystalline sample. For $\sigma(B)$ of an oriented single crystal of U_3Se_5 see Fig. 260. **(b)** Inverse molar magnetic susceptibility, χ_m^{-1}, vs. temperature, T [95S, 99ST]. The solid lines are Curie-Weiss fits with the parameters given in Table F. Inset: thermomagnetic curves yielding T_C = 28 and 24 K for U_3S_5 and U_3Se_5, respectively.

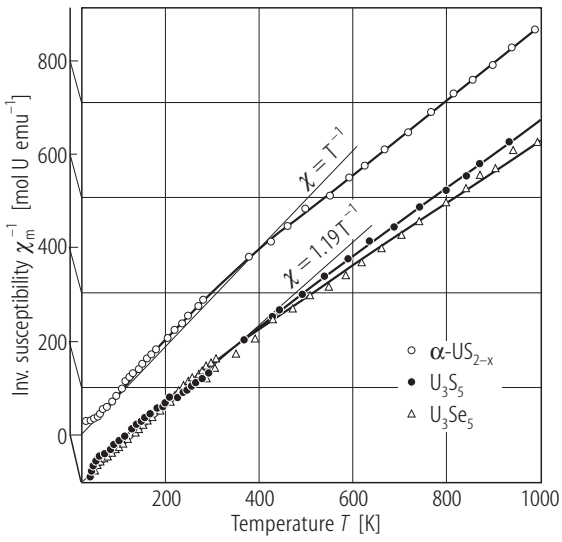

Fig. 252. U_3S_5, U_3Se_5, α-US_{2-x}. Inverse molar magnetic susceptibility, χ_m^{-1}, vs. temperature, T up to 1000 K [74SR]. For all three compounds the $\chi_m^{-1}(T)$ variations are curvilinear. The straight lines mark the Curie law expected for pure crystal field ground states.

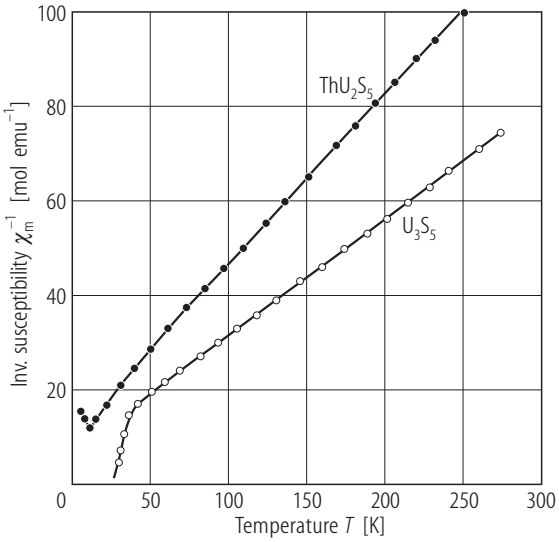

Fig. 253. U_3S_5. Inverse molar magnetic susceptibility, χ_m^{-1}, vs. temperature, T, compared to that of ThU_2S_5 [80NP]. In U_3S_5 a net weak ferromagnetic component associated with the U magnetic moments located on the crystallographic 4(c) sites develops below T_C = 29 K (see Fig. 250). For ThU_2S_5: Θ = –27 K and p_{eff} = 3.34 μ_B. Assuming that in U_3S_5 the contribution of the U^{3+} ions at the 8(d) sites to the effective magnetic moment is also 3.34 μ_B, the contribution of U^{4+} ions at the 4(c) sites can be derived as being 3.10 μ_B. See also Fig. 254.

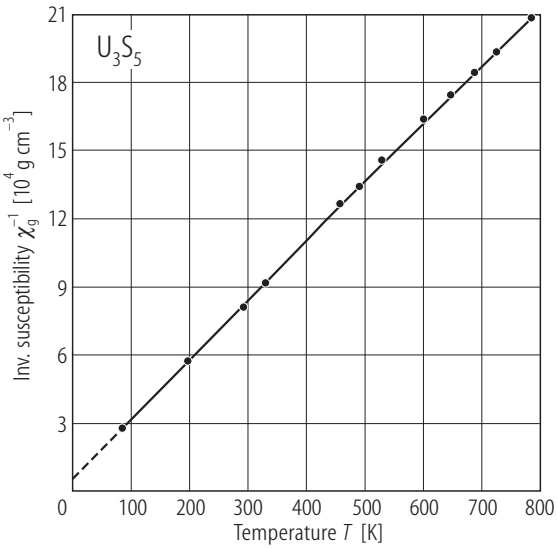

Fig. 254. U_3S_5. Inverse mass magnetic susceptibility, χ_g^{-1}, vs. temperature, T up to 850 K [67CPYM]. The solid line is a Curie-Weiss fit with the parameters: Θ = –16 K and p_{eff} = 3.10 μ_B.

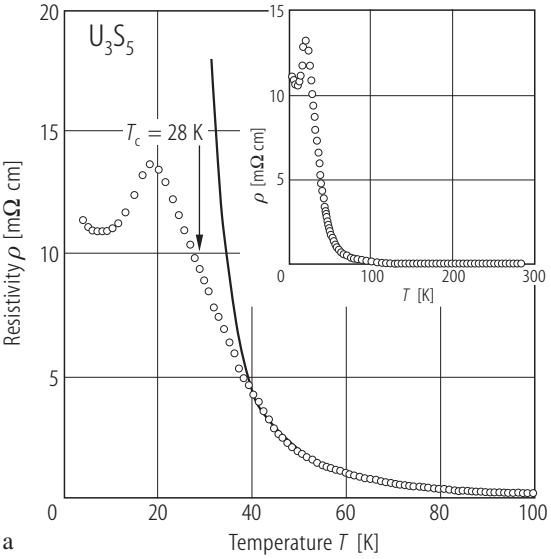

a

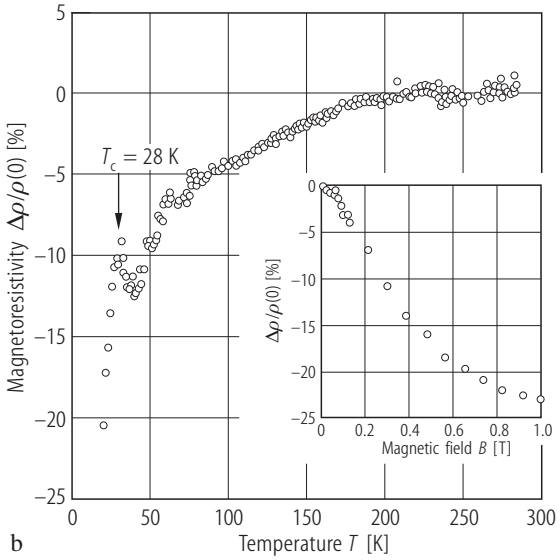

b

Fig. 255. U_3S_5, sc. **(a)** Electrical resistivity, ρ, vs. temperature, T in the range 4.2…100 K and 4.2…300 K (inset) [95S, 99ST]. The solid curve is a fit of the experimental data to the equation $\rho(T)$ [μΩcm] = 0.3 exp(18.9meV/2k_BT) valid in the range 40…100 K. Below T_C = 28 K the energy gap diminishes (see also [94TYKB]). **(b)** Magnetoresistivity, $\Delta\rho/\rho(0)$, vs. temperature, T [95S, 99ST]. Note a high value of MR of about –22% at 4.2 K and a maximum/minimum behaviour around T_C. Inset: $\Delta\rho/\rho(0)$, vs. magnetic field, B, up to 1 T measured at 4.2 K.

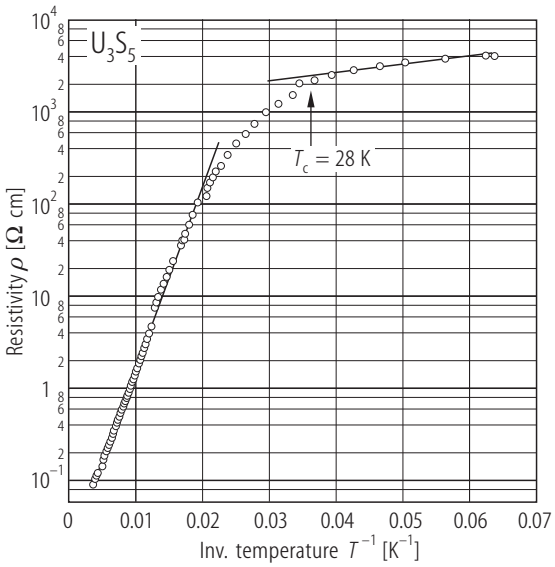

Fig. 256. U_3S_5, sc. Electrical resistivity, ρ, vs. inverse temperature, $1/T$, measured on an aggregate of intergrown crystals [00KB]. ρ(300K) = 94 mΩcm. The compound exhibits semiconducting properties with an energy gap E_g = 78.1(4) meV in the range $50 < T < 300$ K and E_g = 3.4(4) meV below 25 K. The two regions of excitation behaviour are marked by solid lines. The arrow denotes T_C as found by [95STK]. Compare the results presented in Fig. 255. Note that despite the semiconducting behaviour no absorption edge due to a band gap was observed in the optical studies down to 46 meV [00KB].

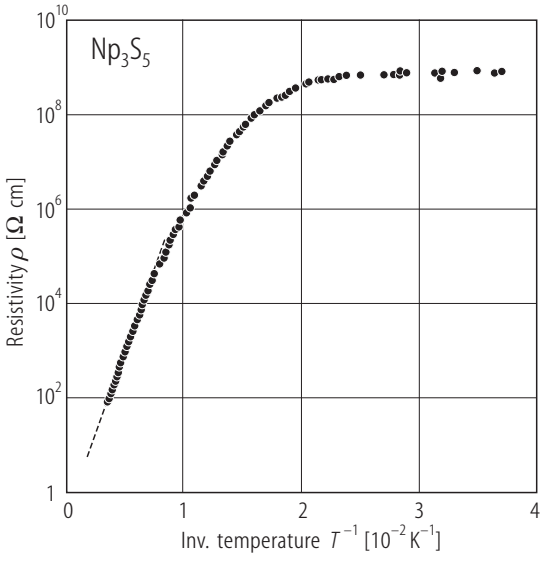

Fig. 258. Np_3S_5. Electrical resistivity, ρ, vs. inverse temperature, $1/T$ [82BDM]. The dashed line marks an activation behaviour observed above 150 K, which yields the thermal activation energy of 0.27 eV. ρ(300K) = 94 Ωcm.

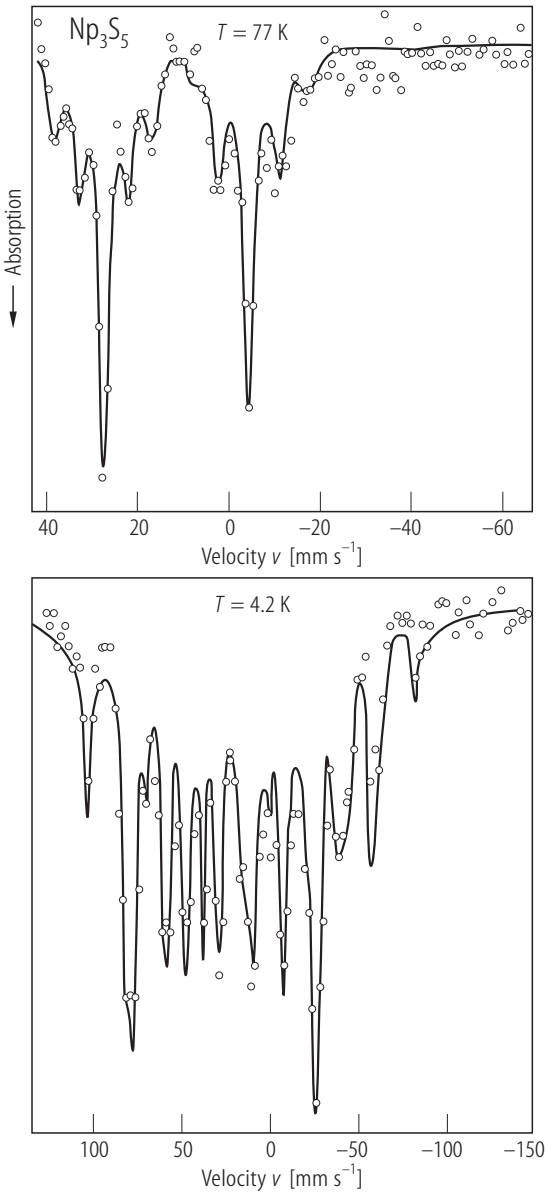

Fig. 257. Np_3S_5. ^{237}Np Mössbauer resonance spectra taken at T = 77 K (upper panel) and 4.2 K (lower panel) [81TJPD]. At 77 K the spectrum exhibits two well defined electric splittings, characterized by the isomer shifts –5(1) and 28(1) mm/s (with respect to $NpAl_2$), which can be assigned to Np^{4+} and Np^{3+} ions, respectively. At 4.2 K the spectrum is more complex because of superposition of electric and magnetic splitting on each Np site. The area ratio of the Np^{4+} and Np^{3+} multiplets is 2.0 yielding two charge states of Np ions according to the formula $Np^{4+}(Np^{3+})_2S_5$.

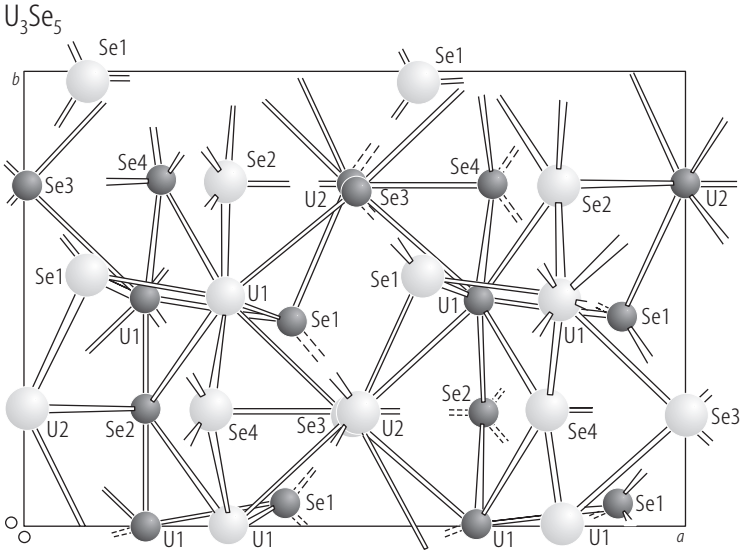

Fig. 259. U_3Se_5, sc. Orthorhombic crystal structure (space group Pnma) viewed down the [001] direction [72MBW]. Small circles: atoms with the positional parameter z close to zero; large circles: atoms with the parameter z approaching unity. The U1 atom is surrounded irregularly by eight Se atoms, while the U2 atom has seven neighbouring Se atoms. The Se1 atom has four near-neigbour U atoms, whereas the Se2, Se3 and Se4 atoms have five such neighbours. The shortest Se-Se distances (340…364 pm) are close to the shortest non-bonding contacts (346 pm) in elemental selenium. The mean values of the U-Se distances are consistent with the ionic composition $(U^{3+})_2U^{4+}(Se^{2-})_5$ proposed by [67M].

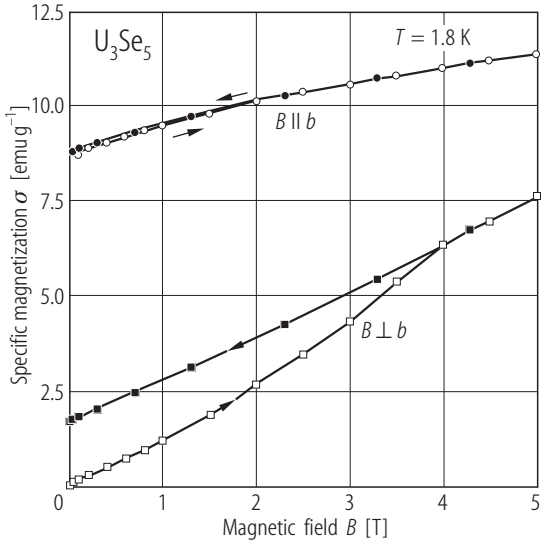

Fig. 260. U_3Se_5, sc. Specific magnetization, σ, vs. magnetic field, B, taken at T = 1.8 K along (circles) and perpendicular (squares) to the crystallographic b-axis [00TKN]. The arrows mark increasing and decreasing magnetic field. For $B \parallel b$ the saturation uranium moment p_s (5T) = 0.85 μ_B.

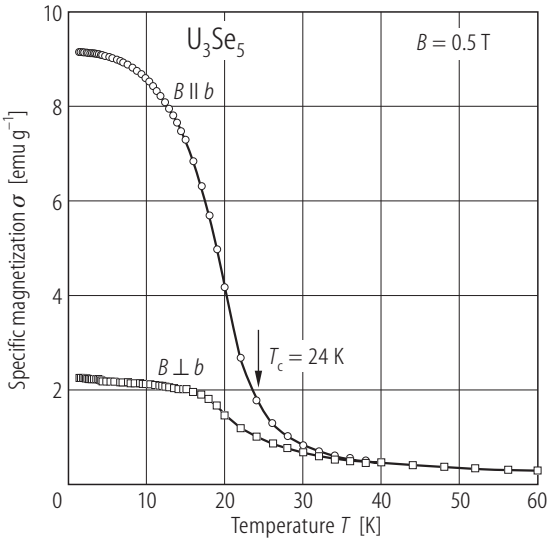

Fig. 261. U_3Se_5, sc. Specific magnetization, σ, vs. temperature, T below 60 K taken in a field of 0.5 T oriented along (circles) and perpendicular (squares) to the crystallographic b-axis [00TKN]. The compound orders ferromagnetically at T_C = 24 K.

Fig. 262 was deleted.

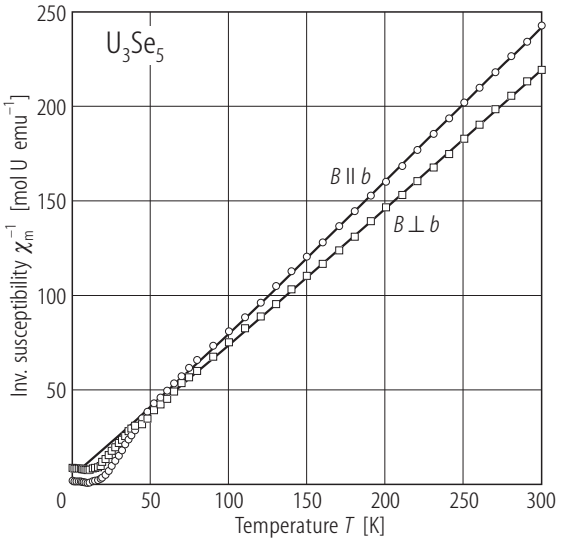

Fig. 263. U_3Se_5, sc. Inverse molar magnetic susceptibility, χ_m^{-1}, vs. temperature, T, measured along (circles) and perpendicular (squares) to the crystallographic b-axis [00TKN]. The solid lines are Curie-Weiss fits with the parameters given in Table F.

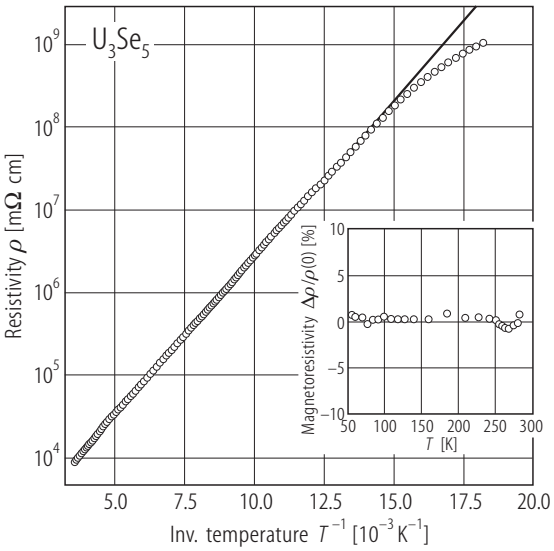

Fig. 264. U_3Se_5, sc. Electrical resistivity, ρ, vs. inverse temperature, $1/T$, measured in the range 50…300 K [99ST]. The solid line shows a fit of the experimental data to the equation: $\rho(T)$ [mΩcm] = 344 exp(151 meV/$2k_BT$). Inset: magnetoresistivity, $\Delta\rho/\rho(0)$, vs. temperature, T, taken in a field of 1 T.

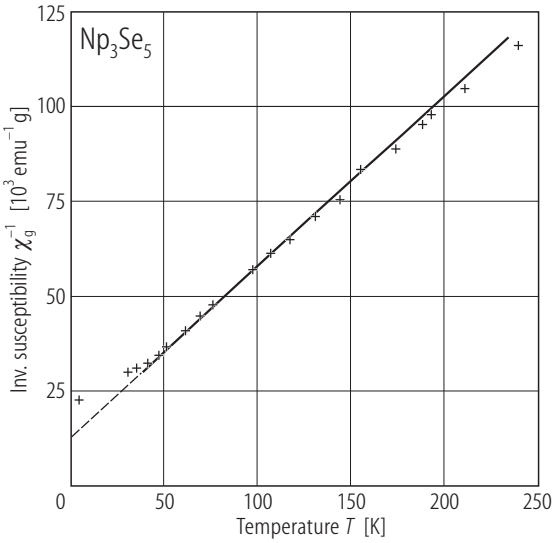

Fig. 265. Np_3Se_5. Inverse mass magnetic susceptibility, χ_g^{-1}, vs. temperature, T [76BFSW]. The solid line is a Curie-Weiss fit with the parameters given in Table F. As in the case of U_3S_5 (see e.g. Fig. 253) one actinide atom is four-valent and two atoms are three-valent. Thus the theoretical effective magnetic moment is $(3.82 + 2 \cdot 2.83)/3 = 3.16\ \mu_B$/Np atom, i.e. nearly equal to the experimental value $p_{eff} = 3.15\ \mu_B$.

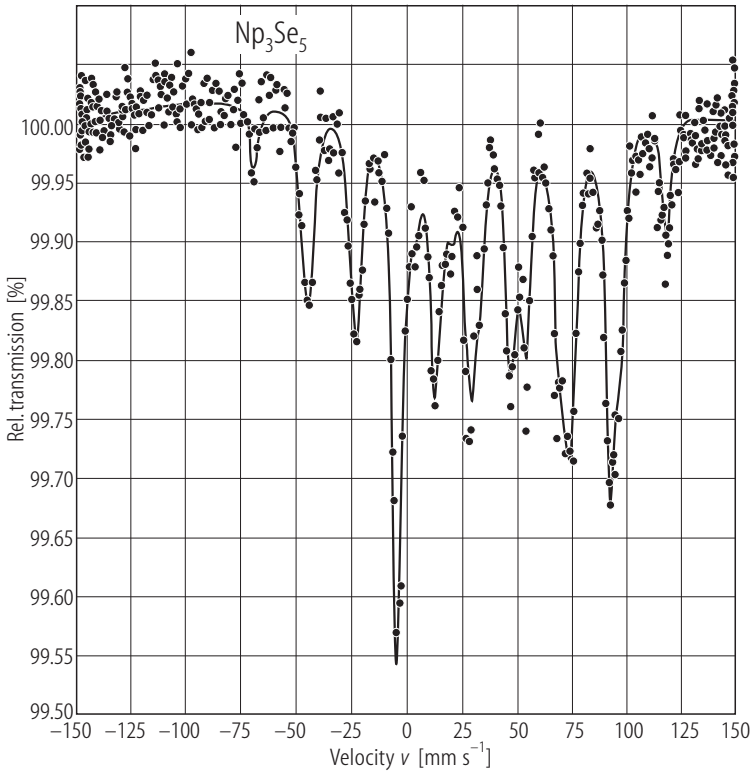

Fig. 266. Np_3Se_5. ^{237}Np Mössbauer absorption spectrum taken at T = 4.2 K [84TJP]. The hyperfine parameters are presented in Table J. Two different isomer shift values were found that indicate two charge states of Np ions in this compound, which can be rationalized as $Np^{4+}(Np^{3+})_2Se_5$, alike the corresponding sulphide (compare Fig. 257).

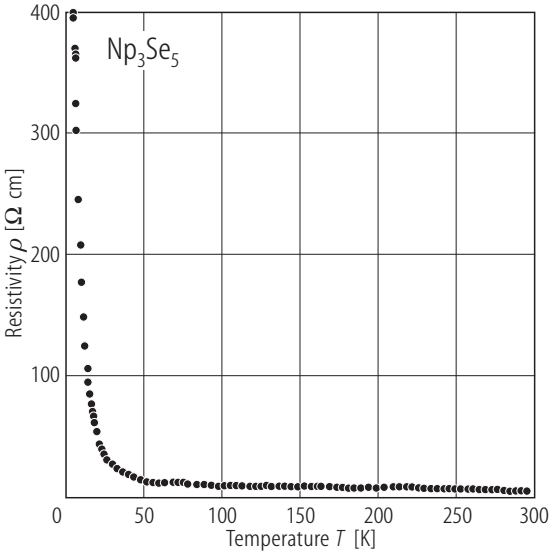

Fig. 267. Np_3Se_5. Electrical resistivity, ρ, vs. temperature, T [82BDM]. ρ(300K) = 5 Ωcm. Below 50 K the resistivity rises sharply but no activation behaviour is observed.

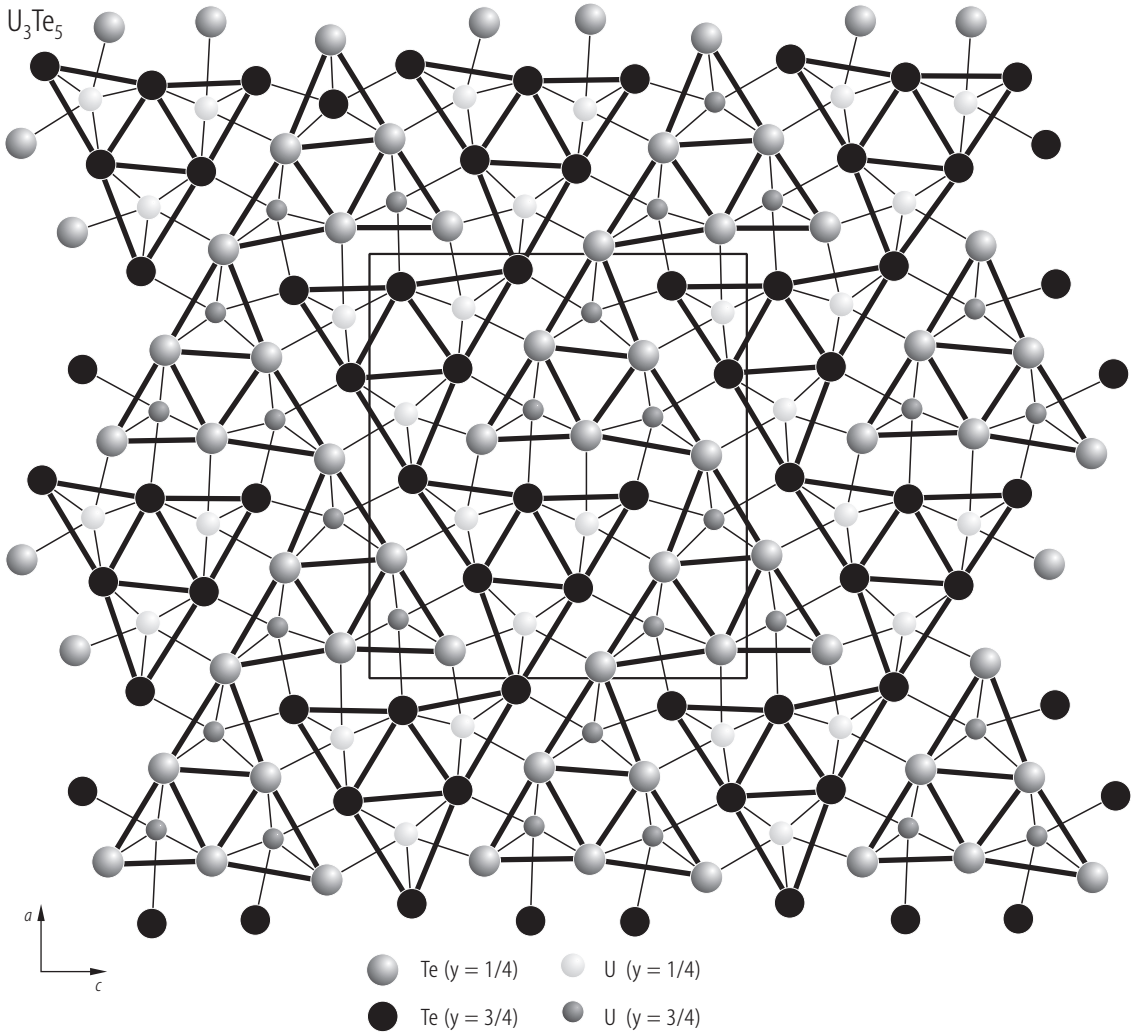

Fig. 268. U_3Te_5. Orthorhombic crystal structure (space group Pnma, related to YCo_5P_3-type) projected onto the (101) plane [98TPN1]. In the unit cell there are three nonequivalent U atoms coordinated to eight Te atoms located in bicapped trigonal prisms. Three such prisms are connected to each other by edge sharing to form a large hexacapped trigonal prism. These large triprisms share their triangular faces along the *b*-axis and are joined by sharing two edges to form finally infinite zigzag chains running in the (*ac*)-planes. The latter are mutually shifted by *b*/2.

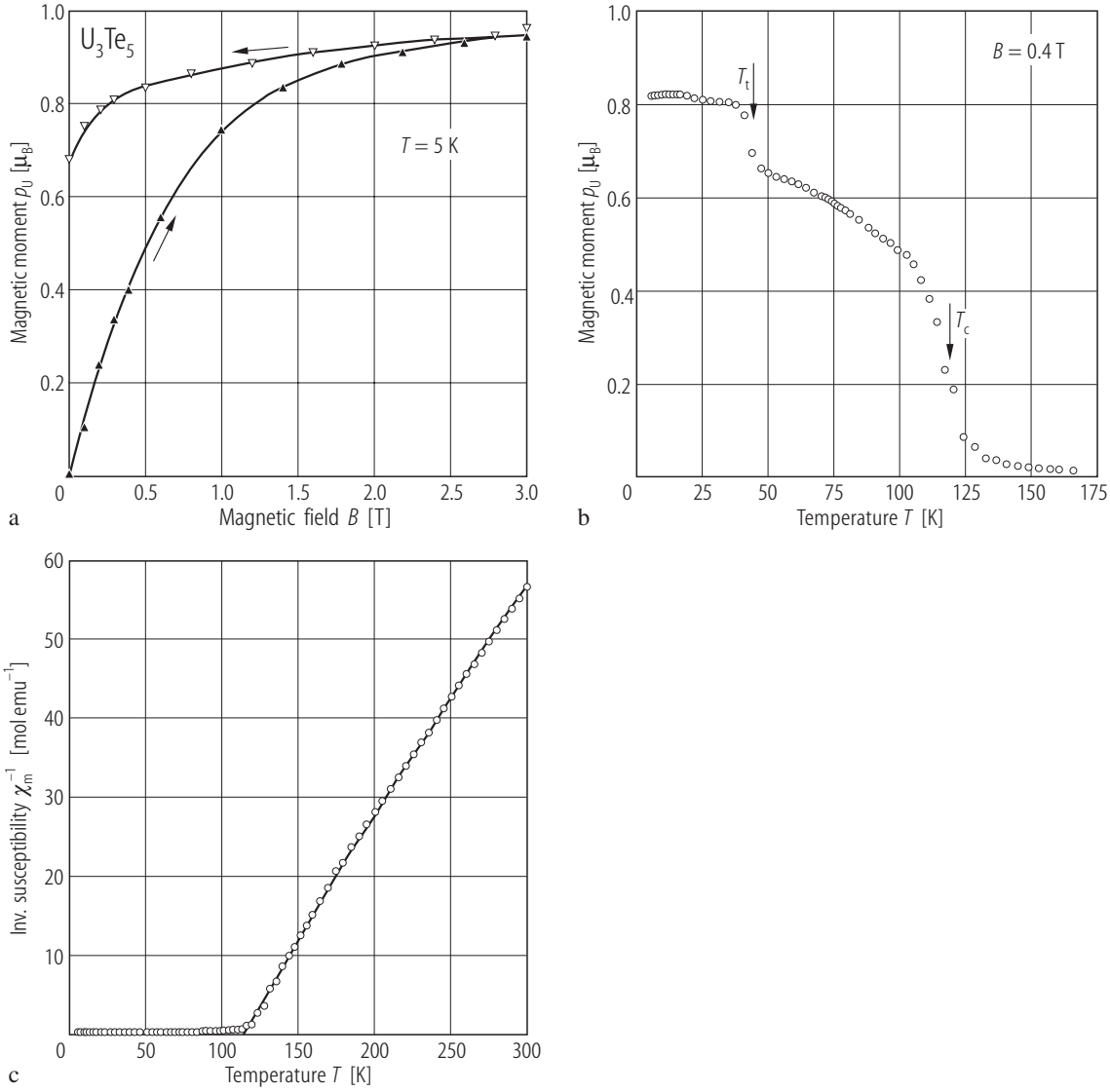

Fig. 269. U_3Te_5. **(a)** Magnetic moment, p_U, vs. magnetic field, B, taken at T = 5 K with increasing (full symbols) and decreasing (open symbols) magnetic field [98TPN1]. The saturation magnetic moment p_s = 0.95 μ_B/U atom. **(b)** Magnetic moment, p_U, vs. temperature, T, up to 170 K [98TPN1]. The compound orders ferromagnetically at T_C = 120 K and undergoes a spin reorientation transition around T_t = 45 K (see Fig. 271). **(c)** Inverse molar magnetic susceptibility, χ_m^{-1}, vs. temperature, T, measured in a field of 0.4 T [98TPN1]. The solid line is a modified Curie-Weiss fit with the parameters given in Table F.

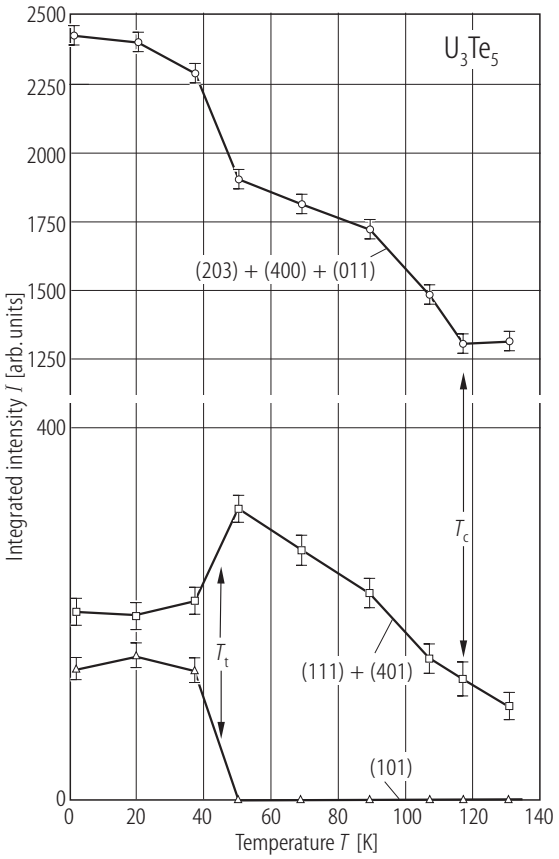

Fig. 270. U_3Te_5. Integrated neutron diffraction intensity, I, of some characteristic Bragg peaks vs. temperature, T, below 130 K [01TABN]. The compound orders magnetically below 115(5) K and exhibits a change in magnetic structure at 45(5) K (see the magnetic structures in Fig. 271).

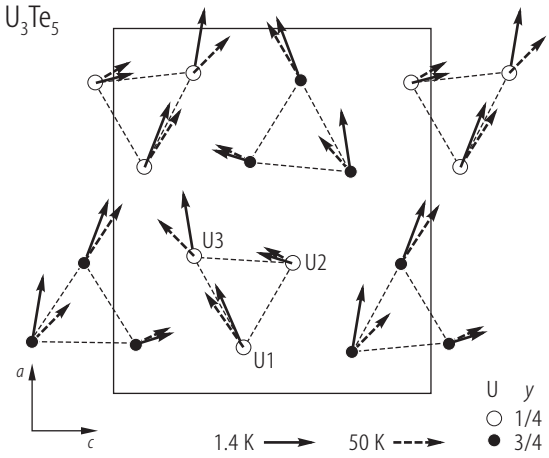

Fig. 271. U_3Te_5. Magnetic structures of the noncollinear F_xC_z-type at 1.4 K (solid arrows) and 50 K (dashed arrows) projected on the (*ac*)-plane [01TABN]. Below T_C = 115 K (see Fig. 269) the magnetic moments on three inequivalent U sites form a complex noncollinear structure with ferro- and antiferromagnetic components within the (*ac*)-plane and have different amplitudes. At 1.4 K, the U1 (1.84 μ_B) and U3 (1.83 μ_B) moments are ferromagnetically coupled and nearly parallel to the *a*-axis, while the U2 (0.98 μ_B) moment is almost aligned along the *c*-axis. At 50 K, the U1 and U2 moments almost keep their alignment, whereas the U3 moment is rotated towards the *c*-axis. The spin reorientation occurs around 45 K (compare Fig. 270).

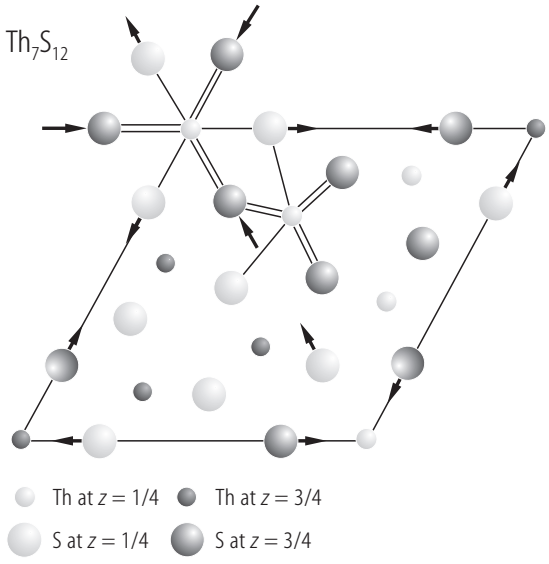

Fig. 272. Th_7S_{12}. Disordered hexagonal crystal structure (space group $P6_3/m$) projected along a six-fold axis [49Z3]. Two of four Th1 atoms are at (0,0,1/4) and the other two at (0,0,3/4). Each Th1 atom is bonded to nine S2 atoms, while each Th2 atom is bonded to five S1 and three S2 atoms. The distances Th1-S2 are either unreasonably short (ca. 260 pm) or large (327 pm) if the Th1 atoms occupy (0,0,1/4) and (0,0,3/4) sites, respectively, and thus the S2 atoms must be shifted from their mean positions. The arrows indicate the directions of such displacements.

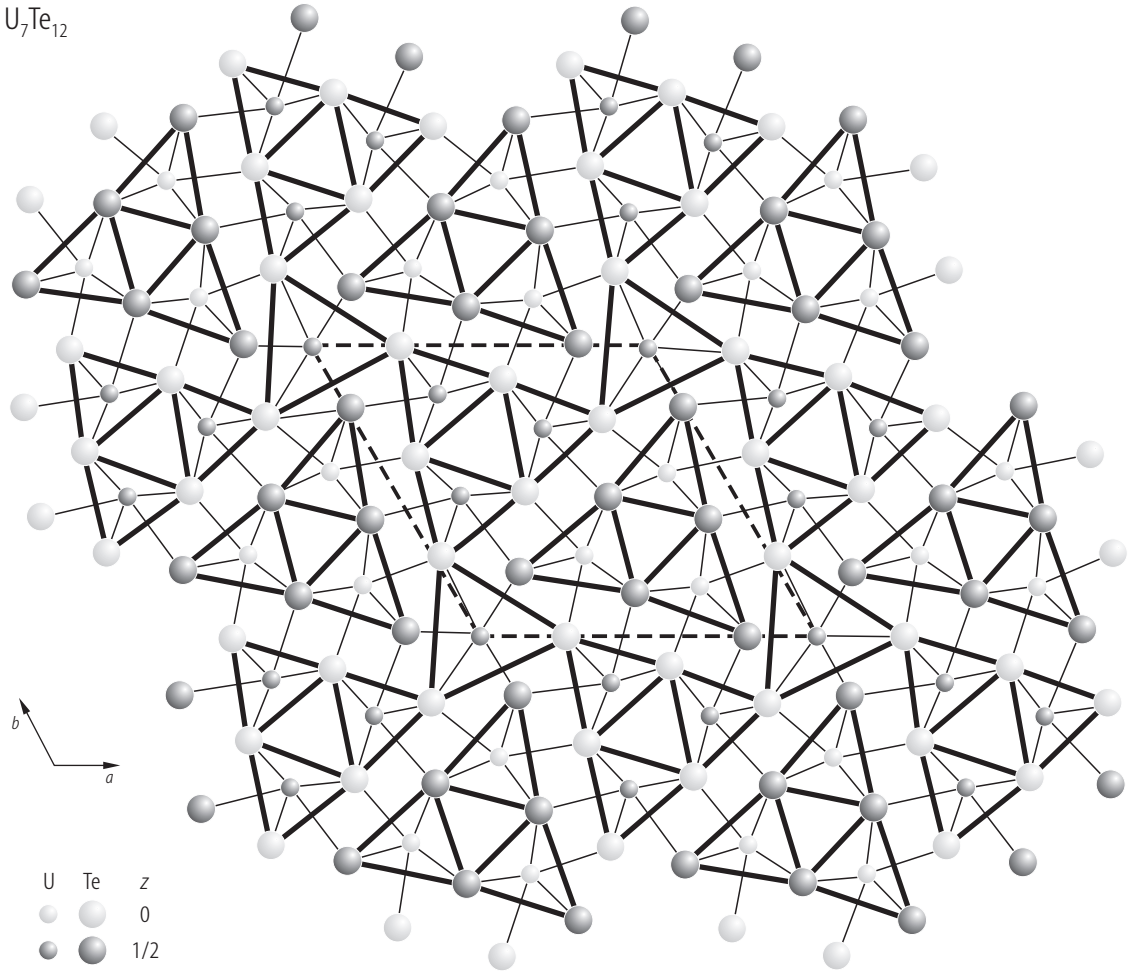

Fig. 273. Th_7Te_{12}, U_7Te_{12}. Hexagonal (space group $P\bar{6}$) crystal structure projected on the (*ab*)-plane [98TPN2]. In the unit cell there are three nonequivalent actinide atoms An1, An2 and An3, which occupy 1(a), 3(k) and 3(j) Wyckoff positions, as well as four nonequivalent Te atoms occupying two 3(k) and two 3(j) positions. The An atoms are placed either in tricapped (An1) or bicapped (An2 and An3) tellurium trigonal prisms. They form infinite columns running along the [001] direction. The trigonal prisms containing An2 and An3 atoms share their edges forming large distorted hexacapped arrangement.

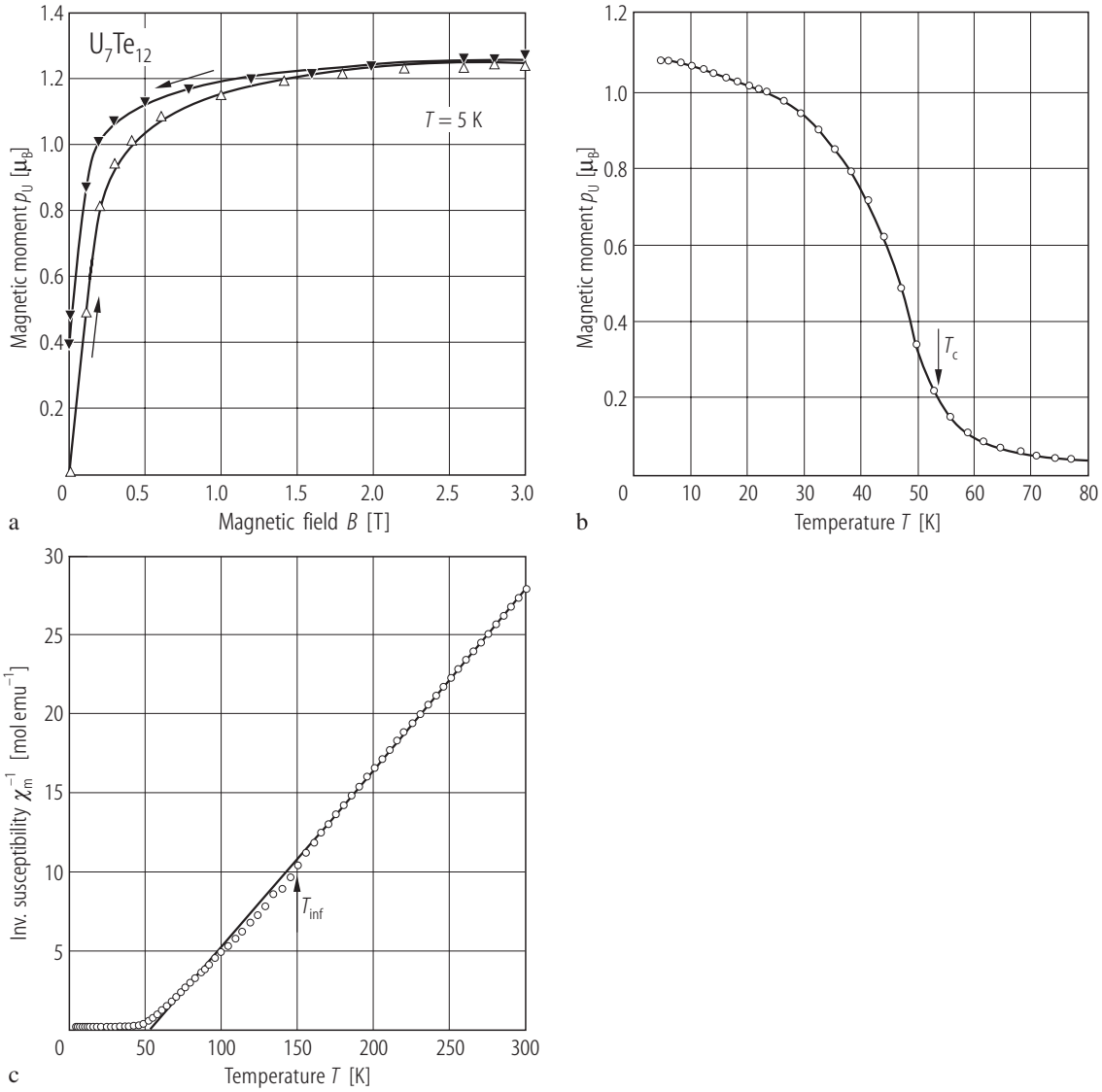

Fig. 274. U_7Te_{12}. **(a)** Magnetic moment, p_U, σ, vs. magnetic field, B, taken at T = 5 K with increasing (open symbols) and decreasing (full symbols) magnetic field [98TPN2]. The saturation magnetic moment is 1.25 μ_B/U atom. **(b)** Magnetic moment, p_U, vs. temperature, T, below 80 K [98TPN2]. The compound orders ferromagnetically at T_C = 54 K. **(c)** Inverse molar magnetic susceptibility, χ_m^{-1}, vs. temperature, T, measured in a field of 0.4 T [98TPN2]. The solid line is a Curie-Weiss fit in the range 80…300K with the parameters given in Table F. The arrow marks an inflection point at about 150 K, which probably indicates the presence of U ions with two different valence states.

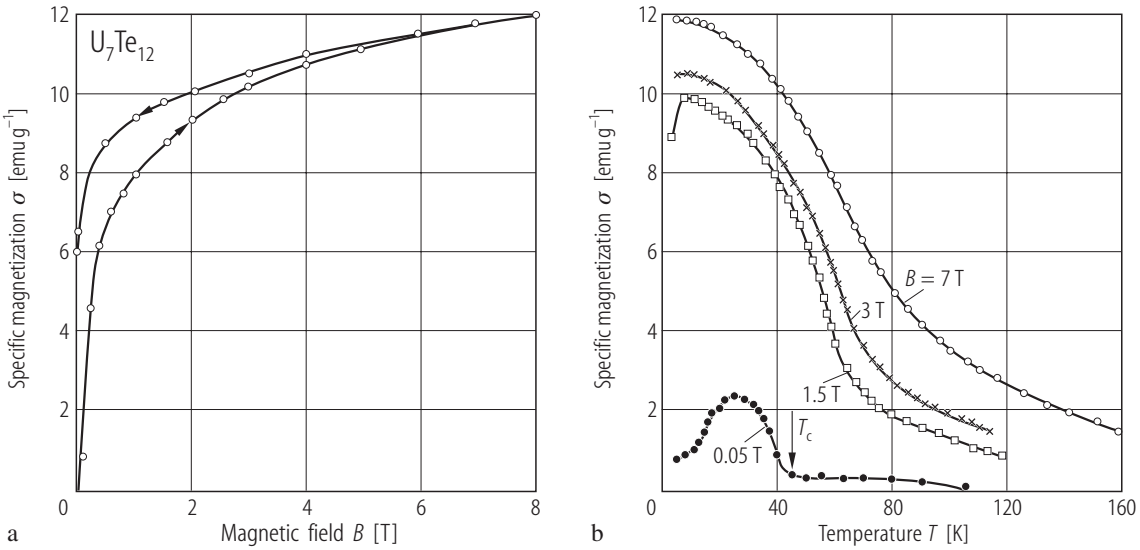

Fig. 275. U_7Te_{12}. **(a)** Specific magnetization, σ, vs. magnetic field, B, up to 8 T taken at T = 4.2 K with increasing and decreasing magnetic field as indicated by the arrows [72S]. Note that in a field of 8 T a saturation is not reached, in contrast to the behaviour of $\sigma(B)$ shown in Fig. 274a. **(b)** Specific magnetization, σ, vs. temperature, T, taken in various magnetic fields from 0.05 to 7 T [72S]. $T_C \approx 50$ K.

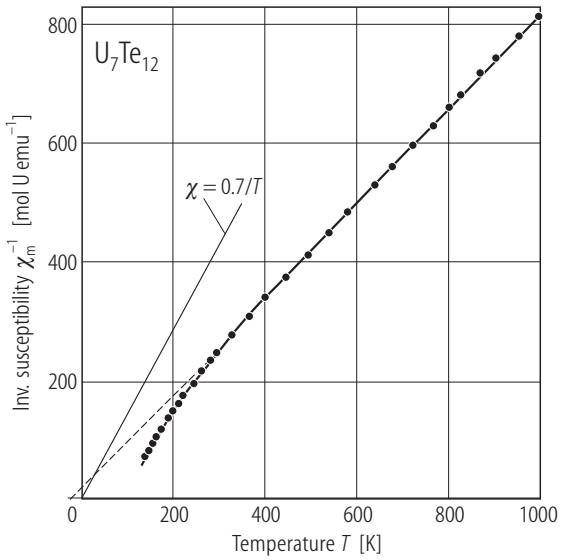

Fig. 276. U_7Te_{12}. Inverse molar magnetic susceptibility, χ_m^{-1}, vs. temperature, T, up to 1000 K [73S]. The solid curve is a Curie-Weiss fit with the parameters given in Table F (compare Fig. 274c). The thin straight line shows the Curie behaviour in the case of two different pseudodoublets as the lowest in energy crystal field levels for U^{4+} ions in both 8- and 9-fold coordinations of Te^{2+} anions.

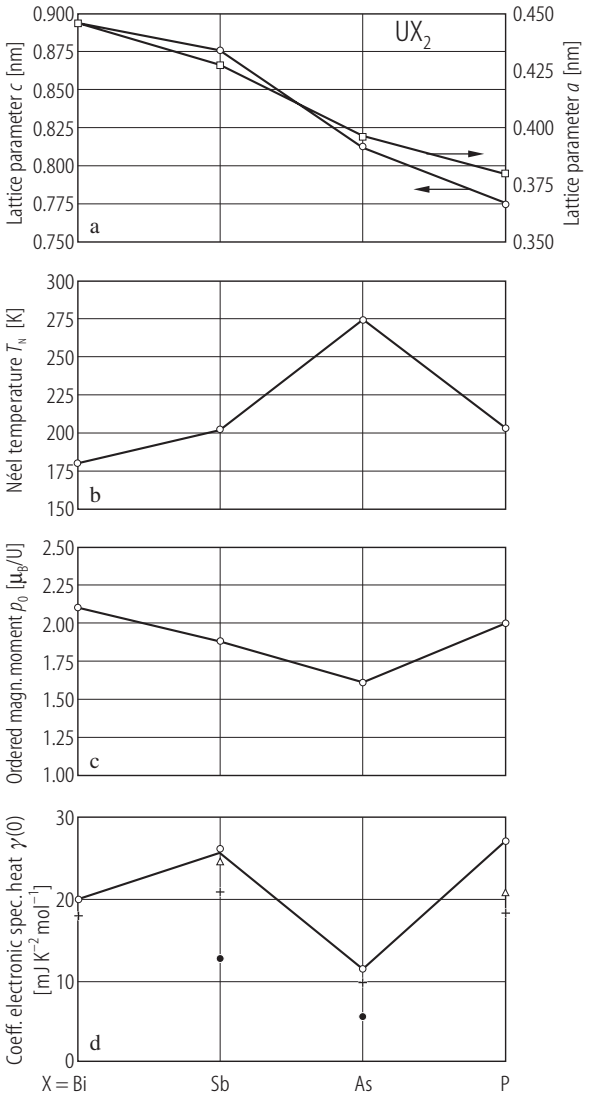

Fig. 277. UX_2, X = P, As, Sb, Bi. General properties: **(a)** lattice parameters, a and c; **(b)** Néel temperature, T_N; **(c)** ordered moment, p_0, found in neutron diffraction studies; **(d)** linear coefficient of the electronic specific heat, $\gamma(0)$ [00AWMW]. The data presented in panel **(d)** were obtained from specific heat measurements (open circles) and de Haas -van Alphen experiments (crosses). Full circles represent specific heat results for UAs_2 and USb_2 taken from [75WSDG], open triangles denote specific heat data for UP_2 and USb_2 taken from [78BFLM].

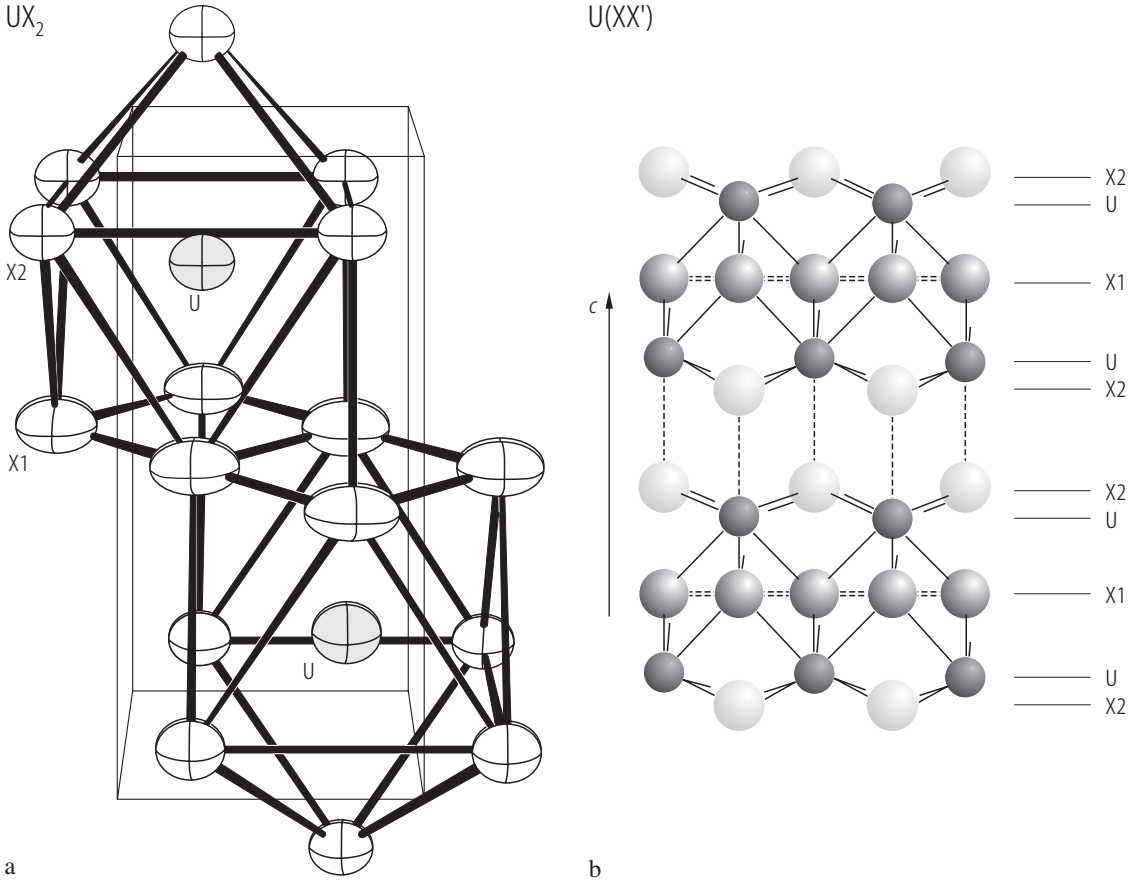

Fig. 278. UX_2, X = As, Sb, Bi. **(a)** Crystal structure [98HCPF]. The structure is of the anti-Cu_2Sb-type (or anti-Fe_2As-type) with the space group P4/nmm. It comprises two interpenetrating tetragonal unit cells, which include two chemical formula units [52I]. The *c*/*a* ratio in this type of structure is always larger than two, in contrast to a similar tetragonal structure of the PbFCl-type. Emphasized are the two coordination polyhedra [$UX1_4X2_5$] around the uranium atoms located at the positions 2(c): ¼, ¼, *u* and ¾, ¾, -*u*, where *u* is about 0.280 (see [67LTMZ]). **(b)** Projection of the crystal structure on the (*ac*)-plane. The structure of the anti-Cu_2Sb-type can be described by successive sheets of actinide atoms (cations) and ligands (anions), which are stacked along the *c*-axis. The positions of ligands (origin at the center of symmetry): X1 - 2(a): ¾, ¼, 0; ¼, ¾, 0 and X2 - 2(c): ¼, ¼, *z*; ¾, ¾, –*z*. The free positional parameter *z* is 0.640 in UAs_2, 0.635 in USb_2 and 0.643 in UBi_2 [67LTMZ]. A characteristic feature of the interatomic distances in the X1-X1 layers is that they approach closely the sum of the covalent radii of coordinating X1 atoms, while those in the X2-X2 layers approach the sum of the ionic radii. This bonding scheme implies the 4+ oxidation state of the central actinide ion, and allows the formation of mixed ternary pnicto-chalcogenides UXY, where the ligands have different valences, and mixed dipnictides UXX', where the ligands have different atomic sizes (see LB III/27 B8).

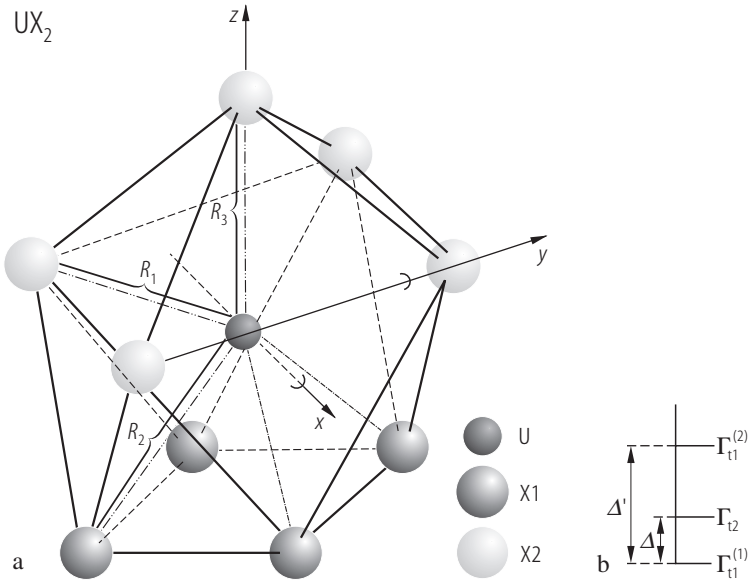

Fig. 279. UX_2, X = P, As, Sb, Bi. **(a)** Ninefold coordination polyhedron around the central uranium atom with the tetragonal C_{4v} point symmetry [72Z]. It can be described as composed of two square pyramids with a common apex formed by the U atom. The X1 and X2 metaloid atoms are situated at the corners of the lower and upper pyramid, respectively. In addition there is a ninth X3 atom placed above the upper pyramid. This coordination together with its slightly distorted derivative is common to many tetragonal and orthorhombic actinide compounds. See Table U for the main interatomic distances. The crystal field Hamiltonian for the uranium ion placed in a potential exhibiting a C_{4v} point symmetry is defined by five CF parameters, B_n^m, and appropriate Stevens equivalent operators, $\hat{O}_n^m$, $\mathbf{H}_{CF} = \sum B_n^m \hat{O}_n^m$, where n = 2, 4 and 6, m = 0 and 4. For details see [84ABM]. **(b)** Crystal field model [84ABM]. The approach assumes a 4+ valency for uranium ions and a Russell-Saunders coupling scheme. Upon splitting the $^3H_4$ ground term in a tetragonal C_{4v} potential, the three lowest lying CF levels are singlets: $\Gamma_{t1}^{(1)}$: $\varepsilon|4\rangle + \gamma|0\rangle + \varepsilon|\bar{4}\rangle$, Γ_{t2}: $\frac{1}{\sqrt{2}}|4\rangle - \frac{1}{\sqrt{2}}|\bar{4}\rangle$ and $\Gamma_{t1}^{(2)}$: $\frac{\gamma}{\sqrt{2}}|4\rangle - \sqrt{2}\varepsilon|0\rangle + \frac{\gamma}{\sqrt{2}}|\bar{4}\rangle$. This phenomenological model has only two adjustable parameters: the energy distance between $\Gamma_{t1}^{(1)}$ and Γ_{t2}, Δ, and the coefficient ε in the eigenfunctions $\Gamma_{t1}^{(1,2)}$. The values of these parameters for UX_2 compounds are given in Table O.

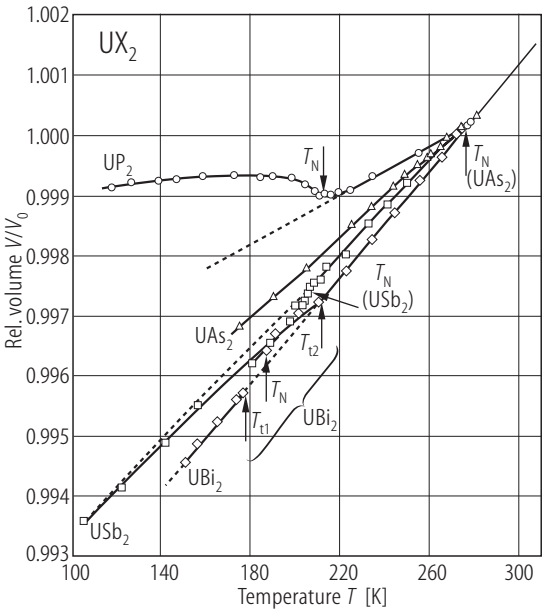

Fig. 280. UX_2, X = P, As, Sb, Bi, sc. Relative volume, V/V_0, vs. temperature T, in the range 110…300 K [77LPKM]. Circles: UP_2; triangles: UAs_2; squares: USb_2; diamonds: UBi_2. The volume thermal expansion of UP_2 is rather small but the anomaly accompanying the AF phase transition is remarkable (see also Fig. 291). On going from UP_2 to UBi_2 the volume thermal expansion coefficients increase but the anomalies at T_N become less pronounced. For UBi_2 the anomaly at T_N is hardly seen but instead the thermal expansion coefficient changes abruptly at the characteristic temperatures T_{t1} and T_{t2}, i.e. below and above T_N, respectively. See also Figs. 291, 308, 344 and 362 for the UX_2 compounds shown separately.

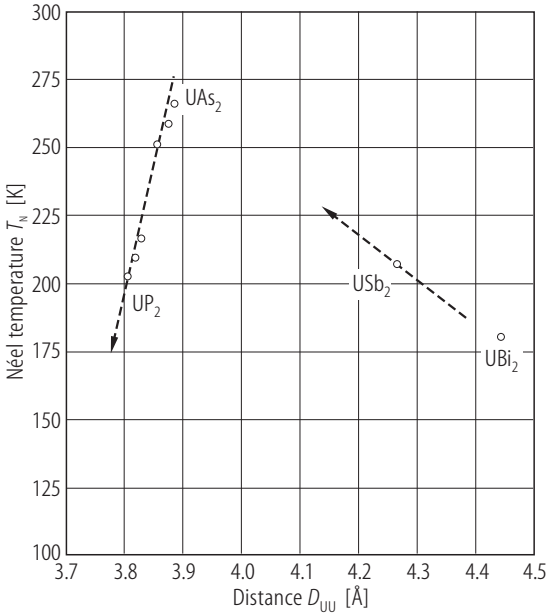

Fig. 281. UX_2, X = P, As, Sb, Bi. Néel temperature, T_N, vs. U-U distance, D_{UU}, in comparison with such a variation for the solid solutions UP_2-UAs_2 [92HMWF]. The data for the solid solutions were taken from [68TM] (see Fig. 323). The dashed arrows mark the direction of change in T_N under pressure.

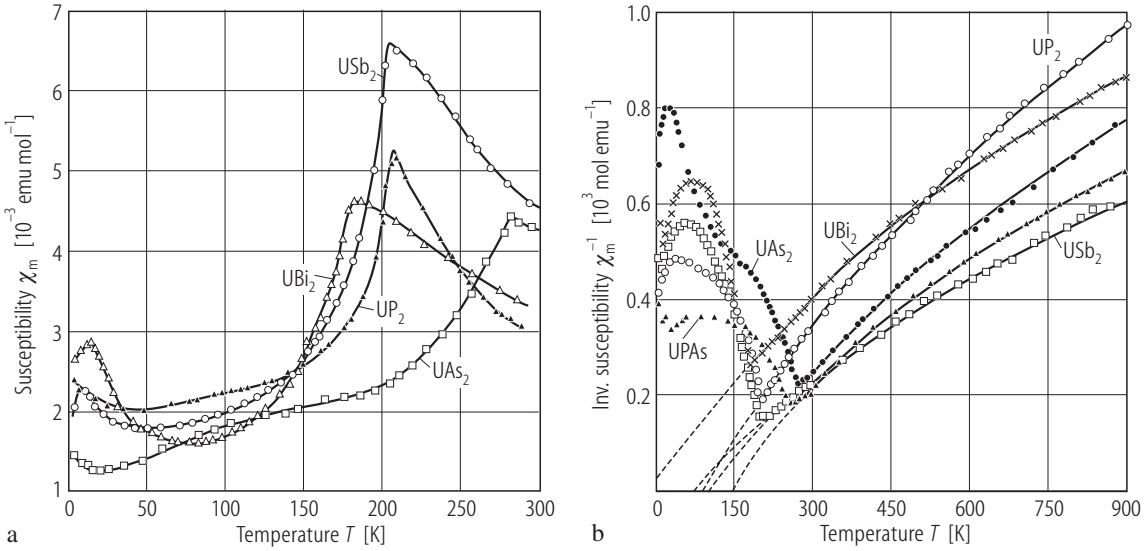

Fig. 282. UX_2, X = P, As, Sb, Bi. **(a)** Molar magnetic susceptibility, χ_m, vs. temperature, T [87T]. Note unusual behaviour of the susceptibility at low temperatures, which presumably results from huge magnetic anisotropy. See Figs. 294, 311, 346 and 363 for the results obtained on single crystals. **(b)** Inverse molar magnetic susceptibility, χ_m^{-1}, vs. temperature, T, up to 900 K [79TZ1, 79TZ2]. For completeness the results for isostructural UPAs are also shown. The lines are fits of the experimental results to the formula $\chi_m^{-1} = \left(\frac{A}{T} + B\right)^{-1} - \lambda$ with the parameters given in Table H.

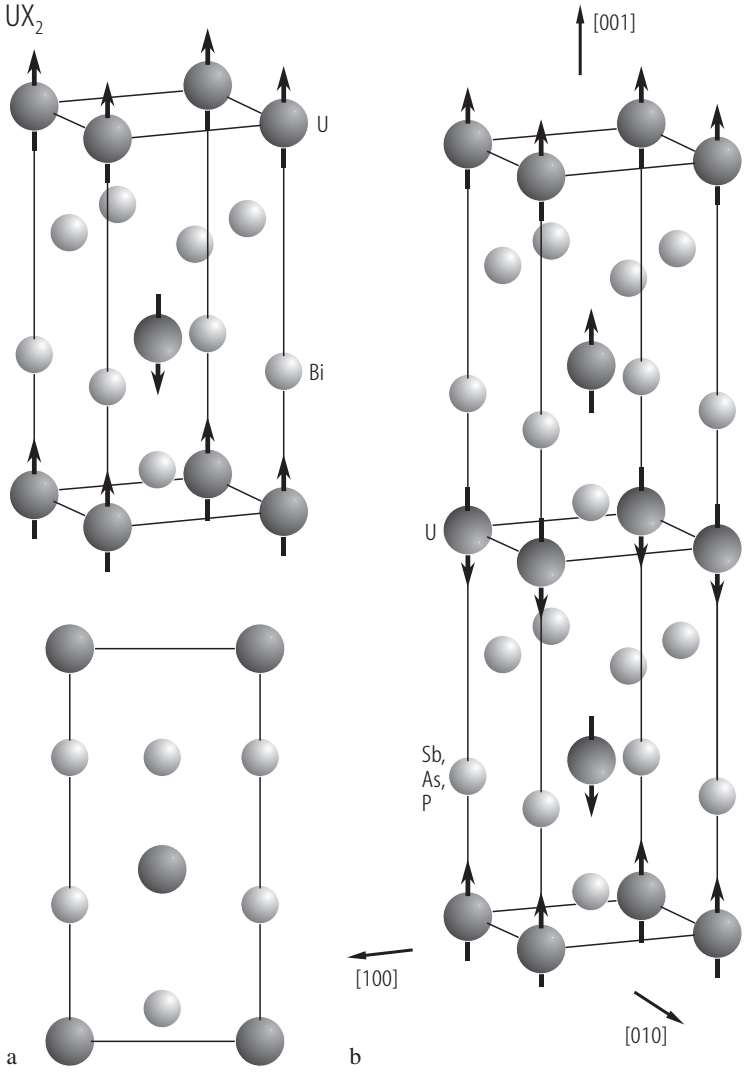

Fig. 283. UX_2, X = P, As, Sb, Bi. Crystal and magnetic structures [00AWMW]. **(a)** UBi_2. The magnetic unit cell is equal to the crystallographic unit cell. The uranium magnetic moments are aligned ferromagnetically in the (001) planes and coupled antiferromagnetically in the + − sequence along the [001] axis. See [67LTMZ] for the magnetic structure determination. **(b)** UX_2 (X = P, As, Sb). The magnetic unit cell is doubled with respect to the chemical cell. The uranium magnetic moments are aligned ferromagnetically in the (001) planes and coupled antiferromagnetically in the + − − + sequence along the [001] axis. The magnetic structures of UP_2, UAs_2 and USb_2 were determined in [66TLC], [65O] and [67LTMZ], respectively.

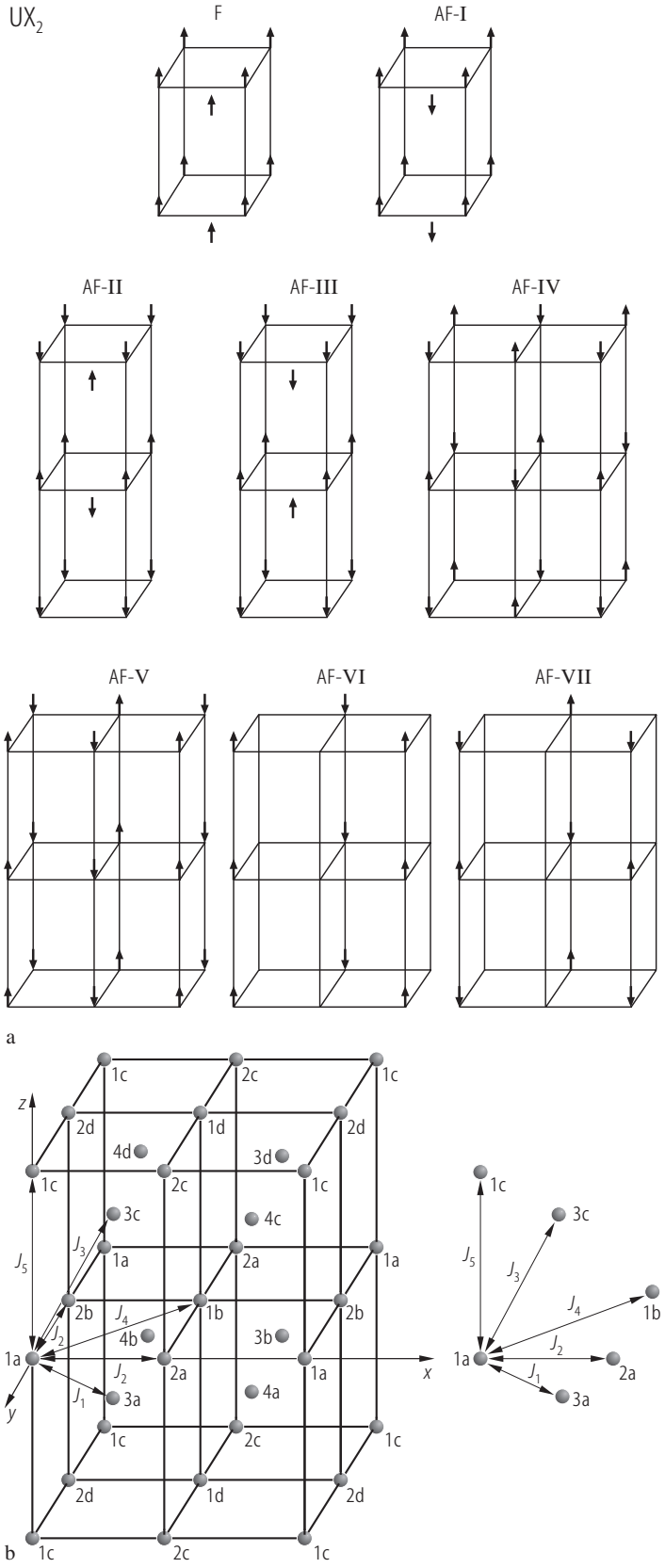

Fig. 284a, b. For caption see next page

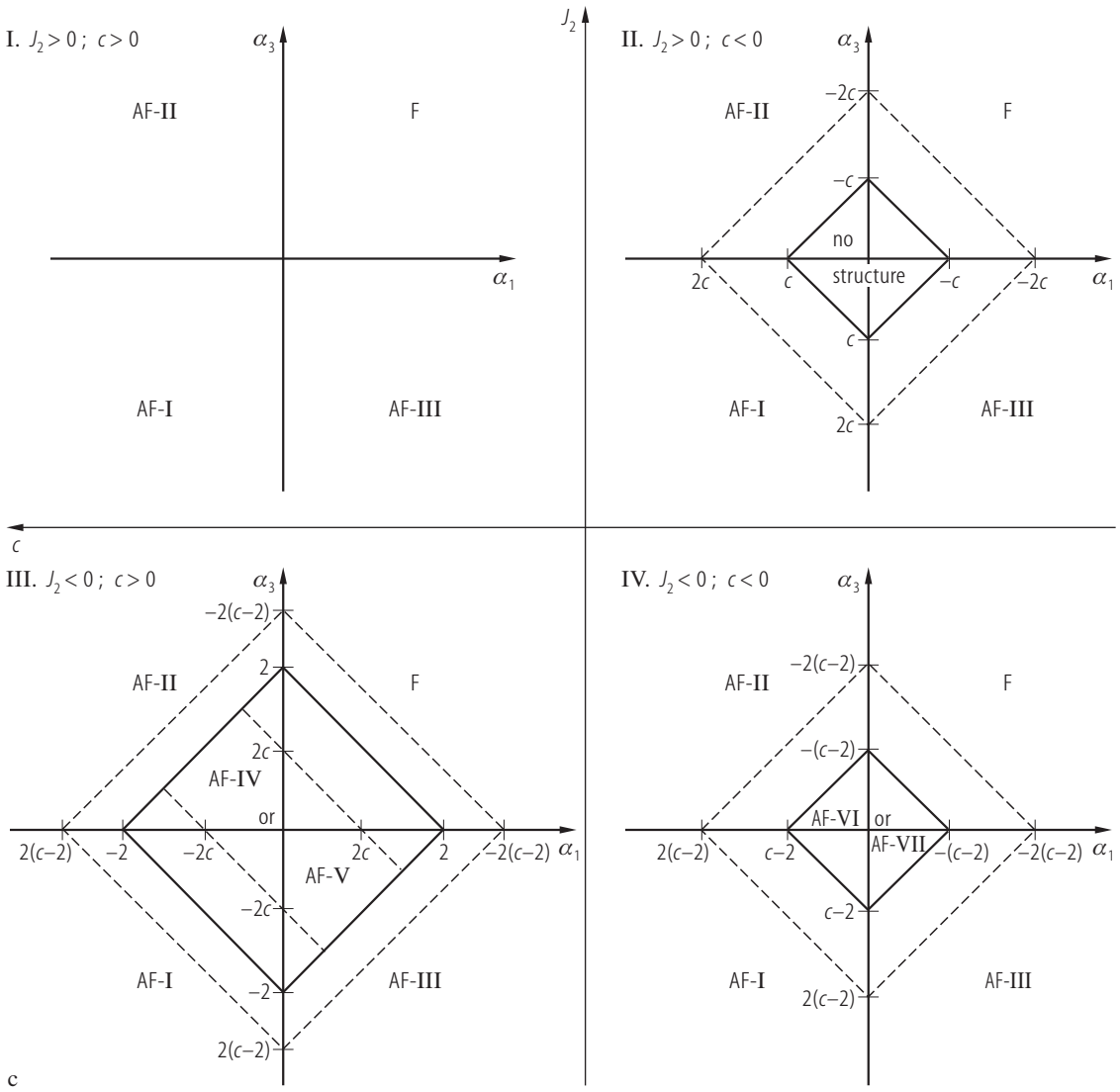

Fig. 284. UX_2. X = P, As, Sb, Bi. **(a)** Possible magnetic structures of the uranium compounds crystallizing with the tetragonal anti-Cu_2Sb-type crystal structure (s.g. P4/nmm), calculated by the Smart's method within the molecular field approximation [67PS]. The five different exchange integrals considered and a division of the crystal structure into sixteen Néel sublattices are shown schematically in panel **(b)**. Among UX_2 compounds the experimentally observed structures are AF-I (UBi_2) and AF-III (UP_2, UAs_2 and USb_2) (see Fig. 283). **(c)** Stability diagram of the structures obtained by the Bertaut's matrix method. The stable structure is the one with the highest critical temperature and $J_5 = 0$. $\alpha_1 = J_1/|J_2|$, $\alpha_3 = J_3/|J_2|$, $\alpha_4 = J_4/|J_2|$, $c = 1 + 2\alpha_4$. It is claimed that the Smart's method admits more collinear structures than the matrix method. For the details see [67PS].

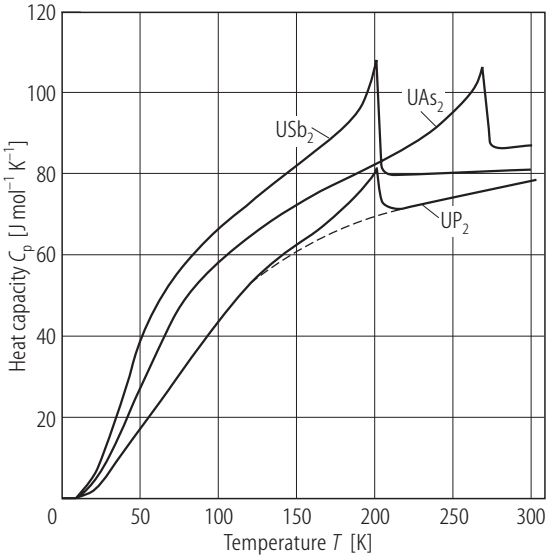

Fig. 285. UX_2, X = P, As, Sb. Heat capacity, C_p, vs. temperature, T [78BFLM]. Sharp λ-shaped peaks manifest second-order antiferromagnetic phase transition at T_N = 202, 270, 201.5 K for UP_2, UAs_2 and USb_2, respectively. The dashed line is a smooth graphical interpolation for the lattice and electronic terms applied for separation of the magnetic contribution to the specific heat of UP_2. Assuming that the phonon contribution is given by a Debye function, the electronic specific heat coefficient $\gamma(0)$ was estimated as 20, 45 and 25 mJ/(mol K^2) in UP_2, UAs_2 and USb_2, respectively. These slightly enhanced values indicate some contribution of the 5f electrons to the total density of states at the Fermi level. Using such a simplified approach the magnetic entropy S_{magn} in UP_2, UAs_2 and USb_2 was estimated as being equal to 1.65, 3.41, 4.65 J/(mol K), respectively.

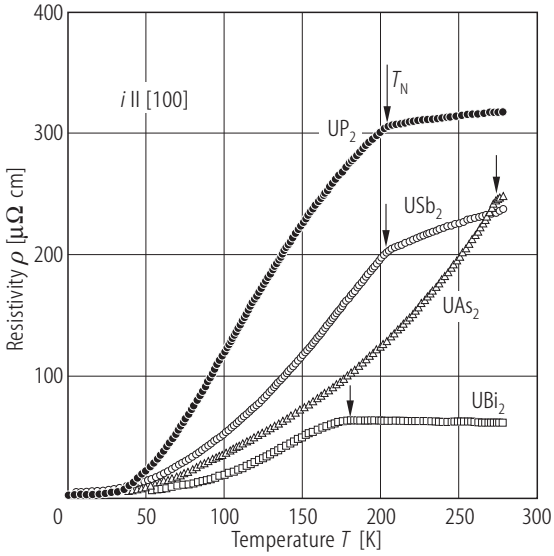

Fig. 286. UX_2, X = P, As, Sb, Bi, sc. Electrical resistivity, ρ, vs. temperature, T, measured with the current flowing along the a-axis [00AWMW]. T_N = 204, 274, 203 and 181 K, respectively, being in good agreement with the relevant magnetic studies of [63TT], [64TSZ] and [66TZ]. Note that the resistivity of UP_2 in the ordered state shows a negative curvature T^n (n < 1) down to 100 K, while the resistivity of the other compounds shows a positive curvature T^n (n > 1) in the whole temperature range below T_N. The residual resistivities ρ_0 are 0.11, 0.29, 2.90 and 2.77 μΩcm and the RRR values are 2900, 500, 21 and 22 for UP_2, UAs_2, USb_2 and UBi_2, respectively.

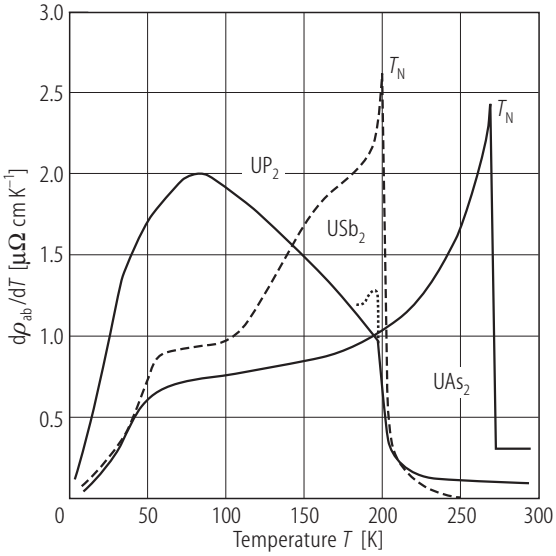

Fig. 287. UX_2, X = P, As, Sb, sc. Temperature derivative of the electrical resistivity measured with the current flowing within the (*ab*)-plane, $d\rho_{ab}/dT$, vs. temperature, T [78BFLM]. Dotted line represents the data for UP_2 taken from [73HK1]. The sharp peaking in $d\rho_{ab}/dT(T)$ at T_N for UAs_2 and USb_2 is in accordance with such a behaviour of $C_p(T)$ for both compounds (see Fig. 312). For UBi_2 a smooth behaviour of $d\rho_{ab}/dT(T)$ near T_N was observed by [73HK1] (not shown).

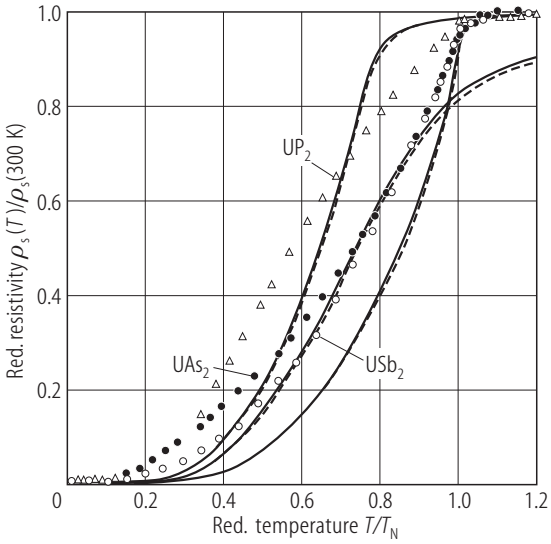

Fig. 288. UX_2, X = P, As, Sb, sc. Normalized spin disorder resistivity, $\rho_s(T)/\rho_s(300K)$, vs. normalized temperature, T/T_N [72HK]. T_N = 203(5), 273(5) and 203(5) K for UP_2, UAs_2 and USb_2, respectively. The solid and dashed lines represent the calculated results obtained for UP_2 and UAs_2, respectively, in the framework of the theory by Kasuya [56K] for various values of the molecular field parameters and the energy gaps of the CF pseudodoublet.

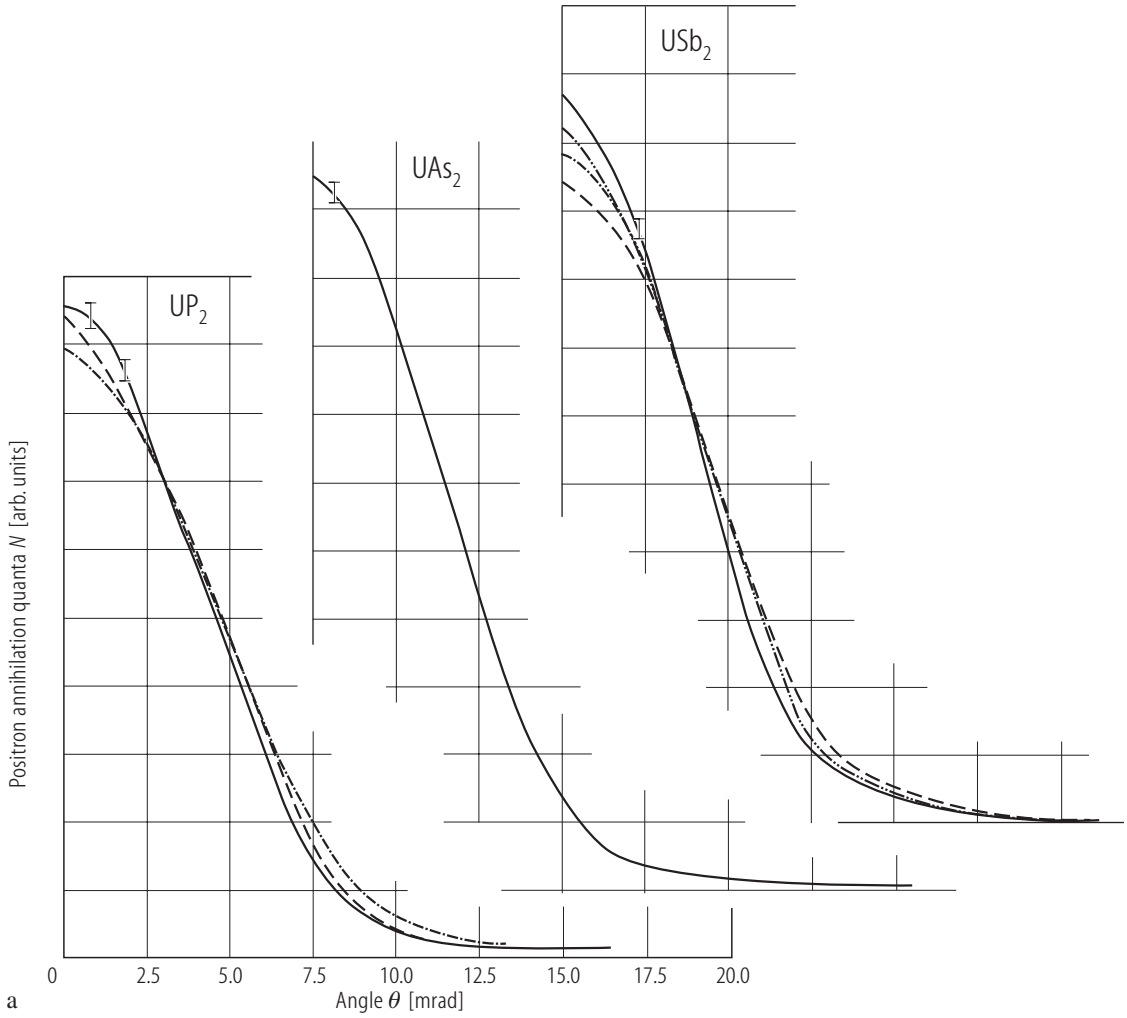

a

Fig. 289a. For caption see next page.

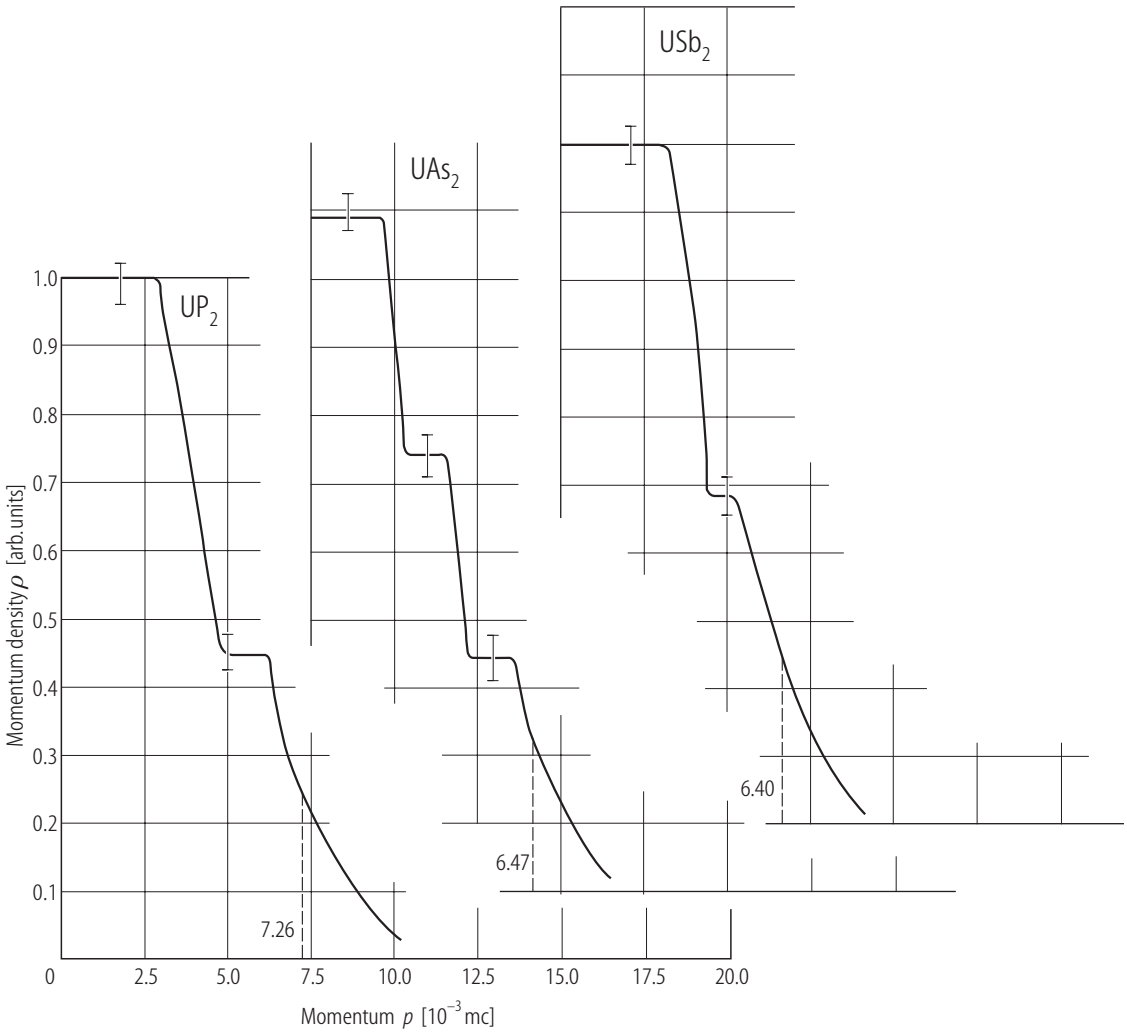

Fig. 289. UX_2, X = P, As, Sb. **(a)** Angular distribution of positron annihilation quanta, $N(\theta)$, normalised to the same area [77RDHW]. Thick solid lines correspond to the results obtained on polycrystalline samples, the other curves were taken on single crystals with various orientations (see the original paper for details). **(b)** Momentum density distribution, $\rho(p)$, obtained from the data shown in panel **(a)** after subtraction core annihilation using Mijnarends' method [77RDHW]. All valence electrons (Z_v) with the maximum momentum p_v are divided into a group of electrons (Z_c) with smaller maximum momenta p_c, which are responsible for metallic-type electrical conductivity, and a group of electrons, which participate in chemical bonding of covalent or ionic character. The values derived from the $\rho(p)$ curves in the framework of the free electron model approximation: $Z_v = 12.6(4)$, $p_v = 7.26(13) \cdot 10^{-3}$ mc, $Z_c = 2.0(4)$ and $p_c = 3.9(4) \cdot 10^{-3}$ mc for UP_2, $Z_v = 10.0(4)$, $p_v = 6.47(13) \cdot 10^{-3}$ mc, $Z_c = 2.8(4)$ and $p_c = 4.2(4) \cdot 10^{-3}$ mc for UAs_2, $Z_v = 12.2(4)$, $p_v = 6.40(13) \cdot 10^{-3}$ mc, $Z_c = 2.5(4)$ and $p_c = 3.8(4) \cdot 10^{-3}$ mc for USb_2. Note that the so-derived numbers of valence electrons are for all three compounds smaller than the sum of valence electrons of constituent elements. On the basis of $\rho(p)$ the cross-sections through the Brillouin zones and Fermi surface were derived for UP_2 (see Fig. 304) and USb_2 (see Fig. 356).

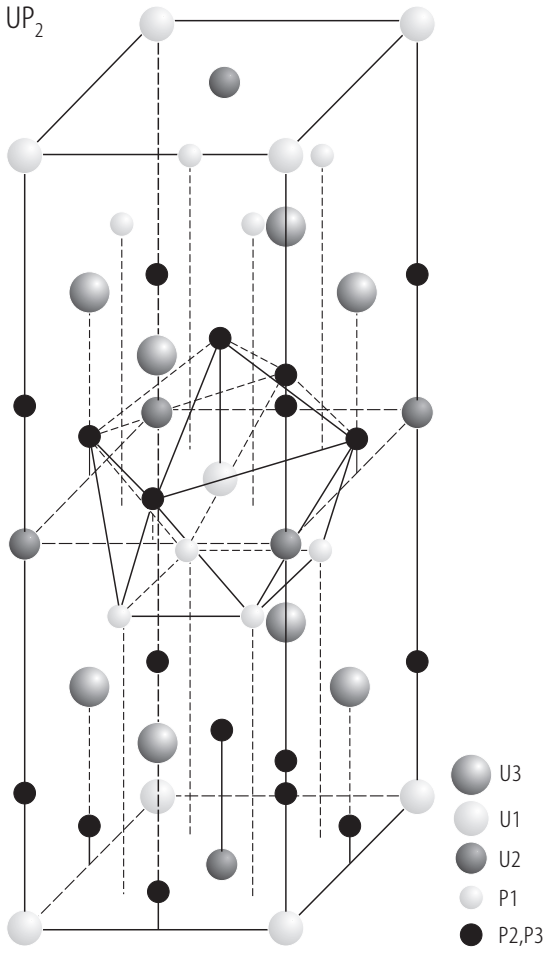

Fig. 290. UP_2, sc. Crystal structure of I4mm space group determined by single crystal X-ray refinement at 300 K [71PL]. Earlier X-ray [52I] and neutron diffraction [66TLC] studies ascribed the structure of UP_2 at RT to the anti-Cu_2Sb-type (space group P4/nmm). The actual unit cell parameters are larger from the previously determined one by a factor $\sqrt{2}$ and 2 for the parameters a and c, respectively. The superstructure unit cell is body centered with eight UP_2 units per cell. A phase transition to the anti-Cu_2Sb-type structure takes place at 358 K, accompanied by a distinct anomaly in $\rho(T)$ (see Fig. 299) and less distinct anomaly in $\chi(T)$ (see Fig. 295). In the Figure the coordination polyhedron around the U1 atom is shown. The coordination polyhedra for the uranium atoms U2 and U3 are similar to that around U1 but their dimensions are significantly different. See also [01WAWS] for a most recent confirmation of the presented crystal structure.

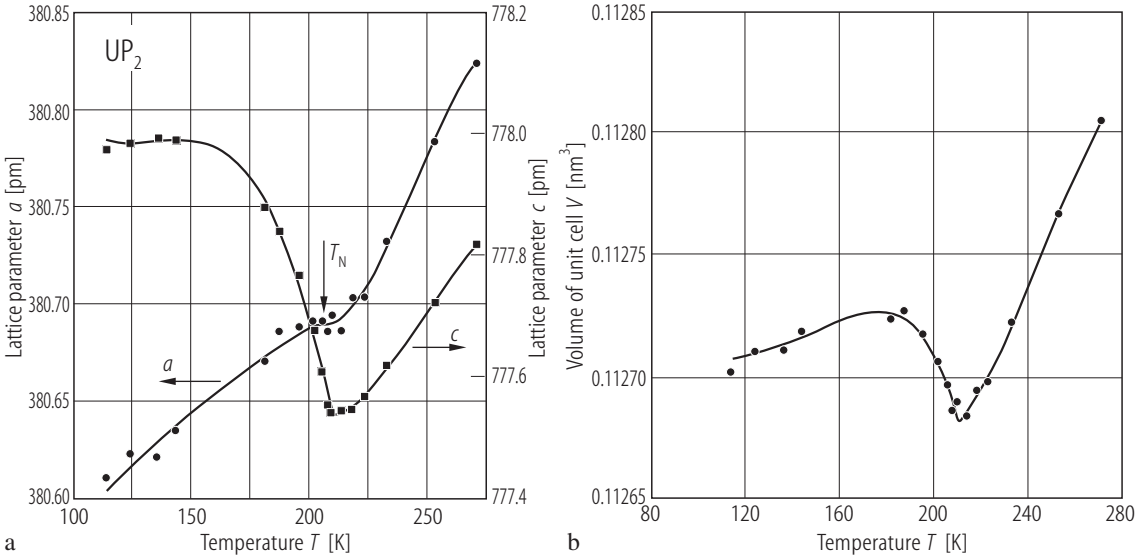

Fig. 291. UP_2, sc. **(a)** Tetragonal lattice parameters, a and c, vs. temperature T, in the range 110…275 K [77PL]. Note a pronounced minimum in the c parameter centered at the Néel temperature $T_N = 209.5$ K and a fairly large anisotropy in the thermal expansion. **(b)** Unit cell volume, V, vs. temperature T [77LPKM]. Note that at T_N there is a remarkable change in $V(T)$, almost absent in the other members of the UX_2 family (compare Figs. 308, 344 and 362).

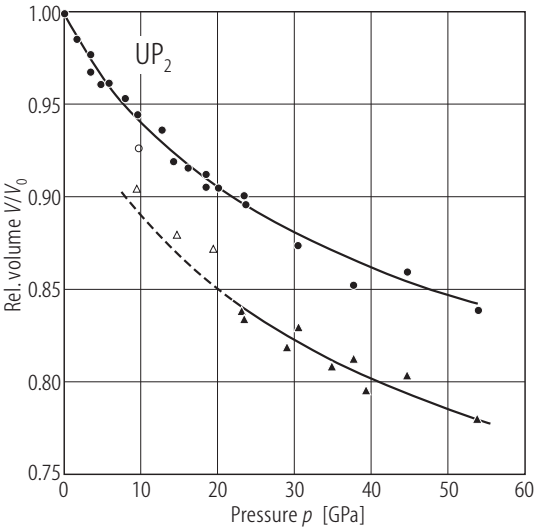

Fig. 292. UP_2. Relative volume, V/V_0, vs. pressure, p, up to 55 GPa [90GSBD]. Circles: tetragonal phase; triangles: orthorhombic phase. Filled symbols: increasing pressure; open symbols: decreasing pressure. A first-order tetragonal-to-orthorhombic phase transformation takes place at about 22 GPa with a 7 % volume contraction. The bulk modulus B_0 = 124(15) GPa, its pressure derivative B_0' = 9(2).

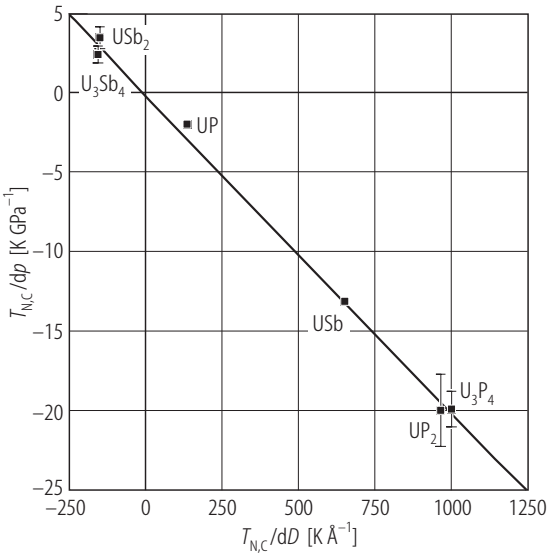

Fig. 293. UX_2, X = P, Sb, sc. Pressure derivative of the ordering temperature, $dT_{N,C}/dp$, vs. the coefficient $dT_{N,C}/dD$, where D is the nearest U-U distance [91HWFM]. The $dT_{N,C}/dD$ values were derived from the data taken from [86HMD] and [68TM]. $dT_{N,C}/dp$ is equal to –20(2) K/GPa and +3.6(7) K/GPa for UP_2 and USb_2, respectively. The high-pressure results are compared to those obtained in [86HMD] for U_3P_4 and U_3Sb_4. Note that the same relation between $dT_{N,C}/dp$ and $dT_{N,C}/dD$ is fulfilled for all four compounds yielding the same absolute linear compressibility dD/dp = 0.0204 Å/GPa (the slope of the straight line).

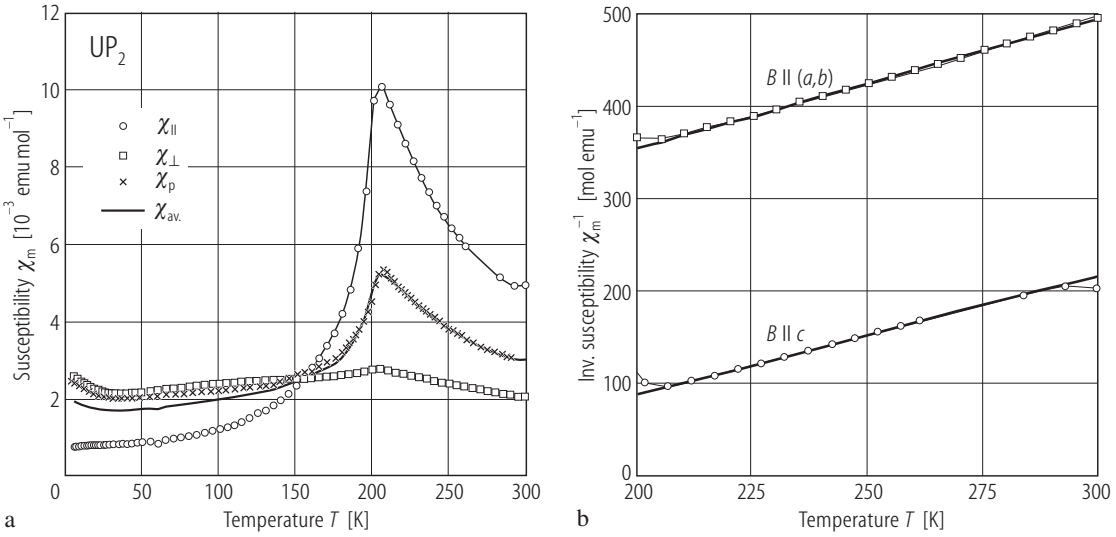

Fig. 294. UP_2, sc. **(a)** Molar magnetic susceptibility, χ_m, vs. temperature, T, measured along the c-axis (open circles) and in the (ab)-plane (open squares) [02TSKP]. The bold solid line represents the average susceptibility $\chi_{av} = (1/3)\ (\chi_{\|} + 2\chi_{\perp})$. For comparison the powder data $\chi_p(T)$ are shown by crosses. Note a rather good agreement between $\chi_{av}(T)$ and $\chi_p(T)$, especially in the paramagnetic region. The compound orders antiferromagnetically at T_N = 203 K. Note a large anisotropy in the magnetic behaviour. **(b)** Inverse molar magnetic susceptibility, χ_m^{-1}, vs. T, measured as in panel **(a)** [02TSKP]. The solid lines are Curie-Weiss fits with the parameters given in Table F.

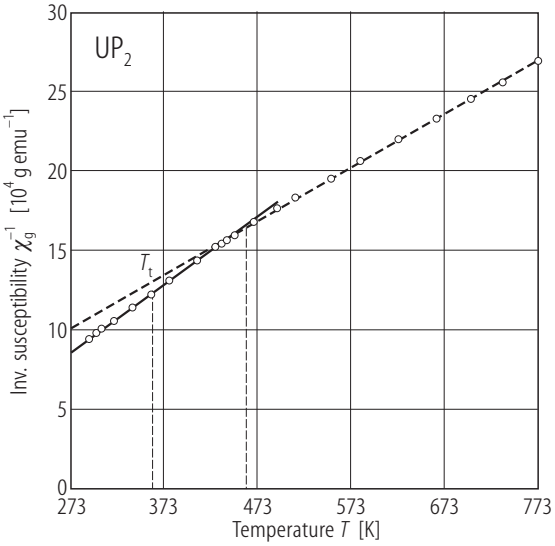

Fig. 295. UP_2. Inverse mass magnetic susceptibility, χ_g^{-1}, vs. temperature, T, in the range 280…800 K [72Z]. The solid and dashed lines are Curie-Weiss fits in the ranges 280…360 K and 460…800 K, respectively, with the parameters given in Table F. The change in the slope of $\chi_g^{-1}(T)$ observed near 360 K is related to a structural transformation from a unit cell of the space group I4mm found for $T < T_t = 358$ K to a unit cell of the space group P4/nmm occurring for $T > T_t$ (see Fig. 278).

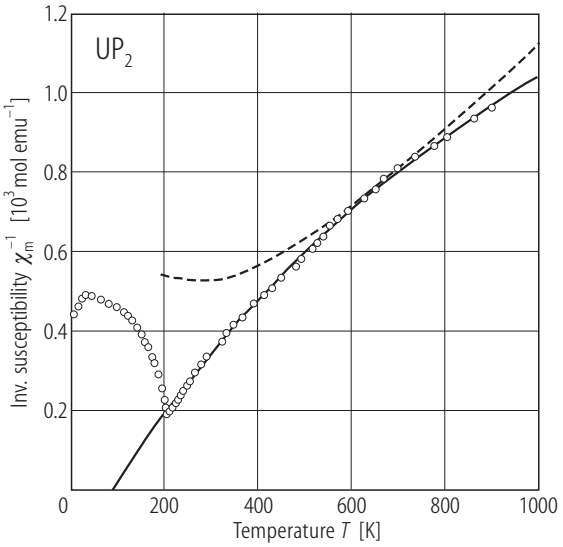

Fig. 296. UP_2. Inverse molar magnetic susceptibility, χ_m^{-1}, vs. temperature, T up to 1000 K, calculated within the crystal field model presented in Fig. 279(b) with the parameters from Table O (dashed line), compared with the experimental data up to 900 K (open circles) [87T]. The solid line is a fit of the experimental results to the formula $\chi_m^{-1} = \left(\frac{A}{T} + B\right)^{-1} - \lambda$ with the parameters: A = 0.486 emu K/mol, $B = 3.32 \cdot 10^{-4}$ emu/mol, λ = –174 mol/emu. Note that the crystal field model from Fig. 279(b) does not give a satisfactory description of the measured $\chi_m^{-1}(T)$.

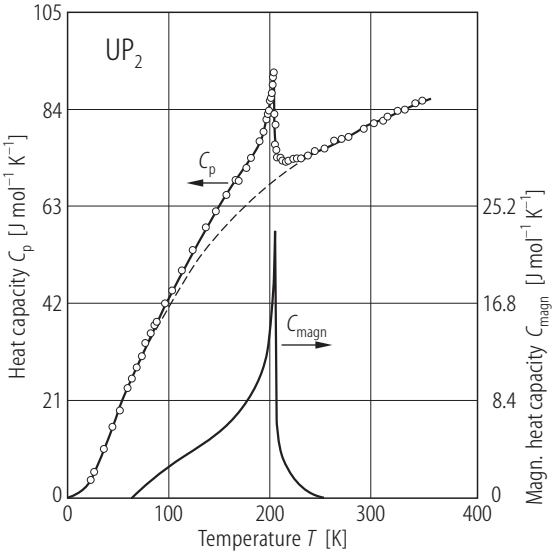

Fig. 297. UP_2. Heat capacity, C_p, vs. temperature, T, in the range 22.5…350.8 K [67SBT]. A sharp λ-shaped peak manifests a second-order antiferromagnetic phase transition at T_N = 203.2 K. The dashed line represents the lattice contribution, C_L, calculated using a combination of three Debye functions with the Debye temperatures of 200, 400 and 700 K, respectively (for details see the original paper). The solid-line curve is the magnetic contribution to the specific heat, C_{magn}, obtained by subtracting from $C_p(T)$ the so-derived $C_L(T)$ plus the electronic contribution, $C_{el} = \gamma T$ = 20.9 mJ/(mol K). The entropy change at the phase transition is ΔS_{magn} = 5.48 J/(mol K), i.e. it is close to Rln2 but considerably smaller than the value of 18.40 J/(mol K) expected for the $5f^2$ configuration (term $^3H_4$) of the U^{4+} ion.

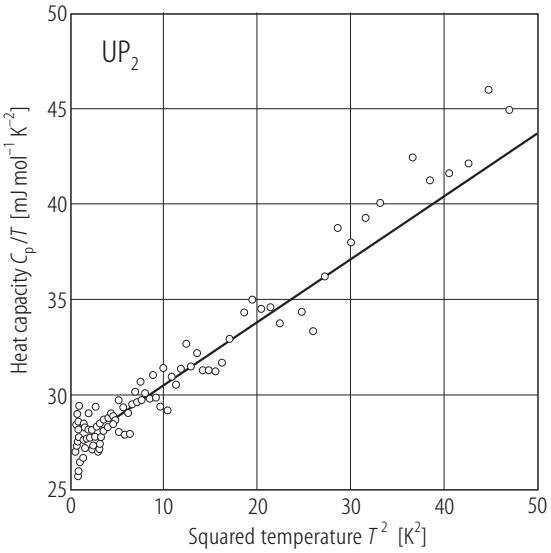

Fig. 298. UP_2. Heat capacity over temperature, C_p/T, vs. squared temperature, T^2, in the range 0.7…7 K [01WAWS]. The solid line is a fit to the expression $C/T = \gamma(0) + \beta T^2$ yielding the electronic specific heat coefficient $\gamma(0) = 27$ mJ/mol K^2.

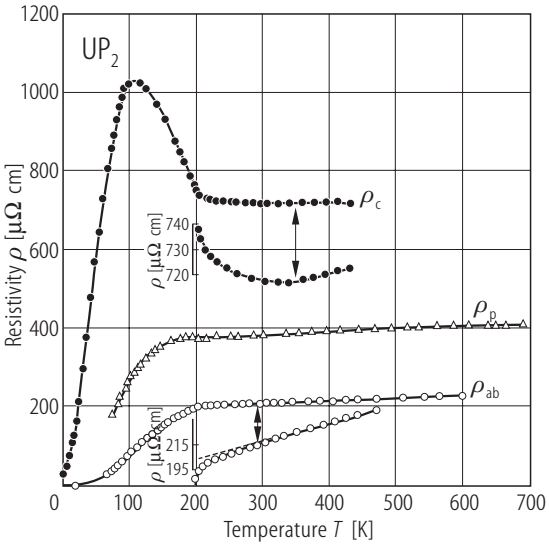

Fig. 299. UP_2, sc. Electrical resistivity, ρ, vs. temperature, T, measured with the current flowing along the c-axis (full circles) and in the (ab)-plane (open circles) [69HT]. For comparison, triangles represent $\rho(T)$ measured on a polycrystalline sample. Note a large anisotropy in the resistivity in both paramagnetic and ordered regions. The antiferromagnetic phase transition at $T_N = 203$ K manifests itself as pronounced kinks in both ρ_c and ρ_{ab}. A large maximum in $\rho_c(T)$ below T_N is due to scattering of conduction electrons on new boundaries in the Brillouin zone. Another anomaly in $\rho_c(T)$ at $T = 358$ K, shown on an enlarged scale in the inset below, is related to a change in the crystal structure (see Fig. 290). At temperatures above 360 K ρ_c increases linearly as $\rho_c = 696 + 0.06T$ [μΩcm] due to electron-phonon scattering. The resistivity in the (ab)-plane has a ferromagnetic-like character in the ordered region and above T_N changes as $\rho_{ab} = 183 + 0.073T$ [μΩcm]. A small change in the slope in $\rho_{ab}(T)$, occurring at $T = 294$ K (see the lower inset) has unknown origin.

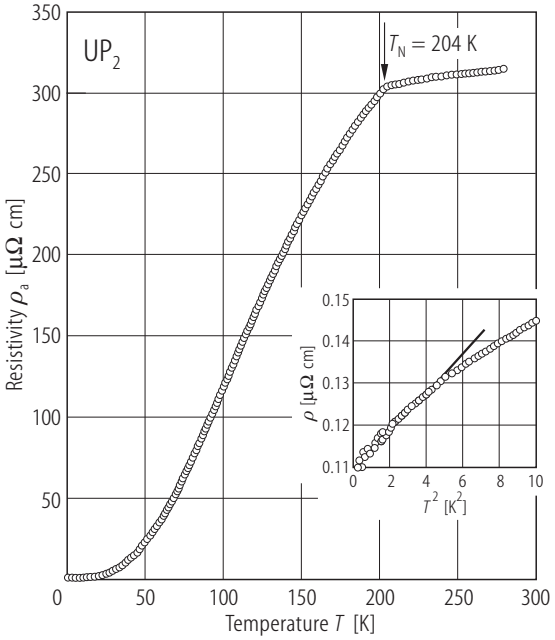

Fig. 300. UP_2, sc. Electrical resistivity, ρ_a, vs. temperature, T, down to 0.1 K measured with the current flowing along the [100] direction [01WAWS]. RRR is as high as 2900, and ρ_0 is only 0.11 μΩcm, both indicating an excellent quality of the crystal measured. A rapid change in slope of $\rho(T)$ occurs at the Néel temperature of 204 K. Inset: Low-temperature $\rho(T)$. The solid line marks a small deviation from a T^2 dependence of the resistivity probed below 2 K.

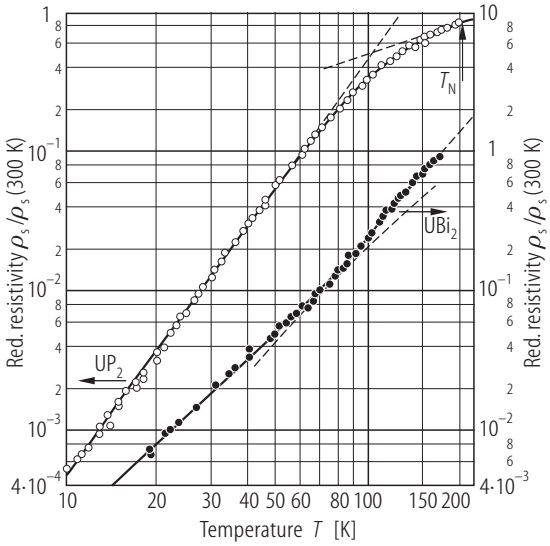

Fig. 301. UX_2, X = P, Bi, sc. Normalized transversal spin-disorder resistivity, $\rho_S/\rho_S(300\ K)$, vs. temperature, T in the range 10…200 K [73HK1]. Open circles: UP_2 (RRR = 500); full circles: UBi_2 (RRR = 250). Note a double logarithmic scale. The values of ρ_S were obtained by subtracting the phonon and residual resistivity from the resistivity measured on single crystals with the current flowing in the (*ab*)-plane. For UP_2, ρ_S is proportional to T^3 in the range 10…60 K and varies as $T^{0.8}$ in the vicinity of T_N = 203 K. For UBi_2, a $T^2\exp(-\Delta/T)$ dependence with Δ = 10 K is observed at low temperatures up to 20 K, a T^2 variation in the range 20…70 K, and finally a $T^{5/2}$ dependence from 70 K up to 165 K (T_N = 184 K). The power law change in $\rho_S(T)$ was attributed to changes in the magnetic anisotropy energy on increasing temperature.

For Fig. 302 see next page

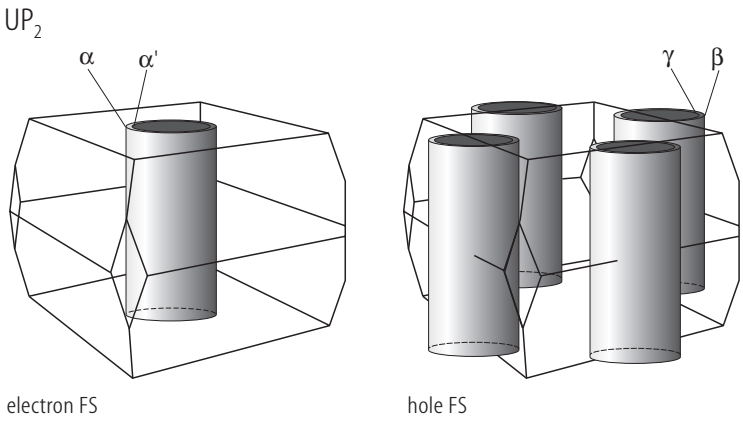

Fig. 303. UP_2, sc. Schematic Fermi surface derived from the Shubnikov – de Haas data given in Fig. 302 [01WAWS]. Note a highly two-dimensional character of cylindrical Fermi surfaces with nearly circular cross sections, which results from flattened Brillouin zone in the magnetically ordered state. It is supposed that the conduction electrons, including itinerant 5f electrons, are confined into the (001) uranium atom sheets in the layered crystallographic unit cell. The proposed scheme of Fermi surface indicates that UP_2 is a compensated metal with equal number of electrons and holes. This yields a good agreement between the calculated total electronic specific heat coefficient $\gamma_s(0) = \gamma_s^{\alpha} + \gamma_s^{\alpha'} + 2\gamma_s^{\beta} + 2\gamma_s^{\gamma}$ = 25 mJ/mol K^2 and the experimental data of 27 mJ/mol K^2 (see Fig. 298).

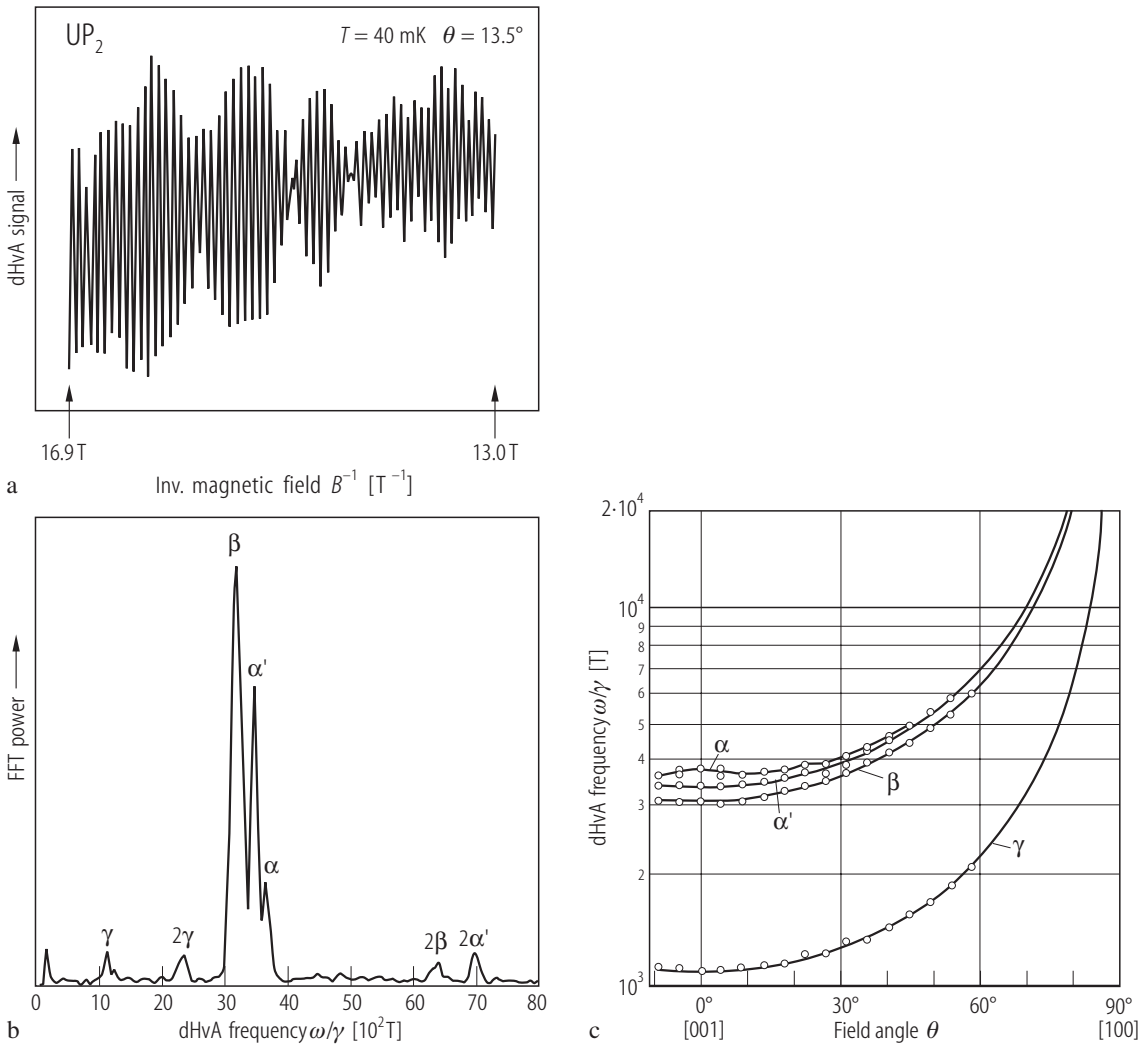

Fig. 302. UP_2, sc. **(a)** Shubnikov – de Haas oscillations measured at $T = 40$ mK in the magnetic field ranging from 13 to 16.9 T tilted by $\theta = 13.5°$ from the [001] axis towards the [100] axis [01WAWS]. **(b)** Fast Fourier transform spectrum corresponding to the data from panel **(a)** [01WAWS]. The presence of four fundamental branches labeled α, α', β and γ in the frequency range from $1.1 \cdot 10^3$ to $3.7 \cdot 10^3$ T were found. The other features are higher harmonics. **(c)** Angular dependence of the SdH frequencies from panel **(b)** [01WAWS]. The solid lines mark a $1/\cos\theta$ variation which is closely followed in the case of branches α', β and γ, indicating the Fermi surface of cylindrical form (see Fig. 303). Note that at $\theta = 30°$ α nearly merges with α'. The effective cyclotron masses (1.9 to 9.3 m_0) are given in Table L. For further details see the original paper.

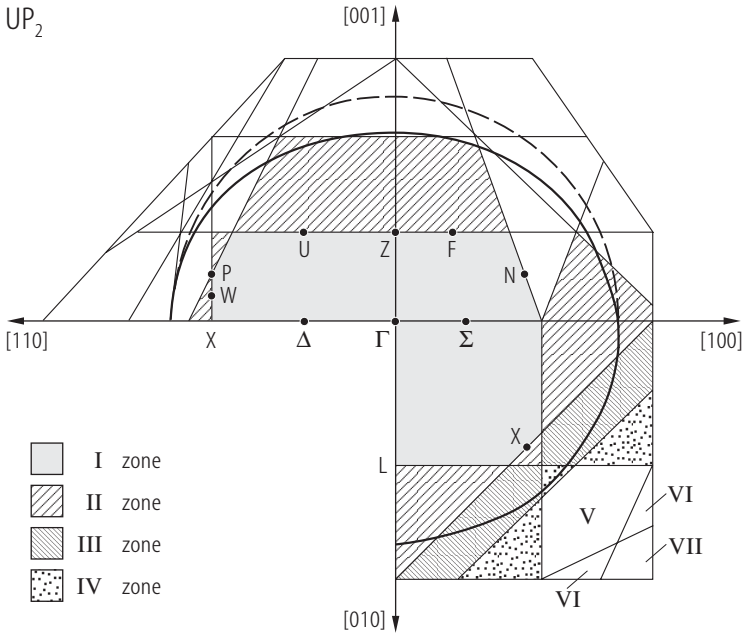

Fig. 304. UP_2. Cross-sections through the Brillouin zones and Fermi surface as derived from the calculated electron momentum density distributions $\rho(p)$ on the basis of the results of the positron annihilation experiments presented in Fig. 289 [80DR]. The dashed curves denote free-electron Fermi sphere. Note an ellipsoidal shape of the Fermi surface flattened in the [001] direction, which is in line with the observed anisotropy in the electrical resistivity (see Figs. 155) as well as with the results of dHvA and SdH studies (see Fig. 299).

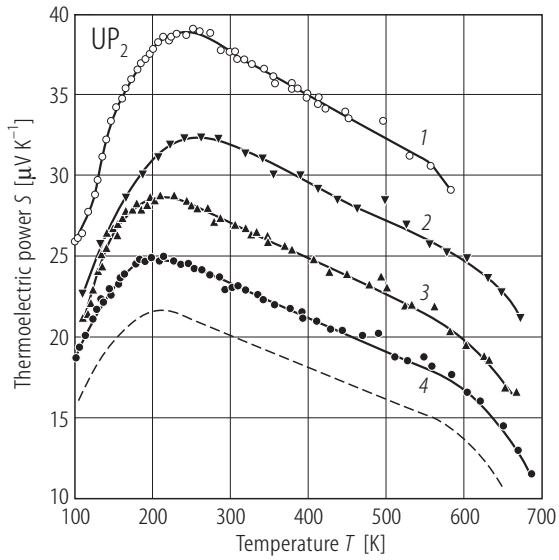

Fig. 305. UP_2, sc. Thermoelectric power, S, vs. temperature, T, in the range 100…700 K, measured in the (*ab*)-plane (1; open circles) and on three different polycrystalline samples (2-4; other symbols) [69HT]. The dashed curve is a hypothetical temperature variation of the thermopower along the *c*-axis (for the details refer to the original paper). Note that the thermopower is rather large as for a case of metallic conductor. The change in slope in $S(T)$ in the vicinity of 200 K is caused by the onset of antiferromagnetic order at T_N = 203 K, whereas such a change near 600 K has unknown origin. The linear decrease in $S(T)$ in the paramagnetic region up to 600 K is mainly due to electron-phonon scattering. The estimated Fermi energy E_F is about 3.2 eV.